

Overdetermined Shooting Methods for Computing Standing Water Waves with Spectral Accuracy

Jon Wilkening^a, Jia Yu^a

^a*Department of Mathematics, University of California, Berkeley*

Abstract

A high-performance shooting algorithm is developed to compute time-periodic solutions of the free-surface Euler equations with spectral accuracy in double and quadruple precision. The method is used to study resonance and its effect on standing water waves. We identify new nucleation mechanisms in which isolated large-amplitude solutions, and closed loops of such solutions, suddenly exist for depths below a critical threshold. We also study degenerate and secondary bifurcations related to Wilton’s ripples in the traveling case, and explore the breakdown of self-similarity at the crests of extreme standing waves. In shallow water, we find that standing waves take the form of counter-propagating solitary waves that repeatedly collide quasi-elastically. In deep water with surface tension, we find that standing waves resemble counter-propagating depression waves. We also discuss existence and non-uniqueness of solutions, and smooth versus erratic dependence of Fourier modes on wave amplitude and fluid depth.

In the numerical method, robustness is achieved by posing the problem as an overdetermined nonlinear system and using either adjoint-based minimization techniques or a quadratically convergent trust-region method to minimize the objective function. Efficiency is achieved in the trust-region approach by parallelizing the Jacobian computation so the setup cost of computing the Dirichlet-to-Neumann operator in the variational equation is not repeated for each column. Updates of the Jacobian are also delayed until the previous Jacobian ceases to be useful. Accuracy is maintained using spectral collocation with optional mesh refinement in space, a high order Runge-Kutta or spectral deferred correction method in time, and quadruple-precision for improved navigation of delicate regions of parameter space as well as validation of double-precision results. Implementation issues for GPU acceleration are briefly discussed, and the performance of the algorithm is tested for a number of hardware configurations.

Keywords: water waves, standing waves, resonance, bifurcation, Wilton’s ripples, trust-region shooting method, boundary integral method, spectral deferred correction, GPU acceleration, quadruple precision

Contents

1	Introduction	2
2	Equations of motion and time-stepping	3
2.1	Equations of motion	4
2.2	GPU-accelerated time-stepping and quadruple precision	5
2.3	Translational and time-reversal symmetry	7
3	Overdetermined shooting methods	7
3.1	Nonlinear least squares formulation	8
3.2	Adjoint continuation method	9
3.3	Trust-region shooting method	10
4	Numerical results	11
4.1	Standing waves of unit depth	12
4.2	Nucleation of imperfect bifurcations	13
4.3	Degenerate and secondary bifurcations due to harmonic resonance	14
4.4	Breakdown of self-similarity and the Penney and Price conjecture	18
4.5	Counter-propagating solitary waves in shallow water	21
4.6	Gravity-capillary standing waves	22
4.7	Performance comparison	24
5	Conclusion	25
A	Boundary integral formulation	28
B	Linearized and adjoint equations for the water wave	29
C	Levenberg-Marquardt implementation with delayed Jacobian updates	30

1. Introduction

Time-periodic solutions of the free-surface Euler equations serve as an excellent benchmark for the design and implementation of numerical algorithms for two-point boundary value problems governed by nonlinear partial differential equations. In particular, there is a large body of existing work on numerical methods for computing standing waves [1, 2, 3, 4, 5, 6, 7, 8] and short-crested waves [9, 10, 11, 12] for performance comparison. Moreover, many of these previous studies reach contradictory scientific conclusions that warrant further investigation, especially concerning extreme waves and the formation of a corner or cusp. Penney and Price [13] predicted a 90 degree corner, which was verified experimentally by G. I. Taylor [14], who was nevertheless skeptical of their analysis. Grant [15] and Okamura [16] gave theoretical arguments supporting the 90 degree corner. Schwartz and Whitney [1] and Okamura [8] performed numerical experiments that backed the 90 degree conjecture. Mercer and Roberts [2] predicted a somewhat sharper angle and mentioned 60 degrees as a possibility. Schultz *et al.* [7] obtained results similar to Mercer and Roberts, and proposed that a cusp may actually form rather than a corner. Wilkening [17] showed that extreme waves do not approach a limiting wave at all due to fine scale structure that emerges at the surface of very large amplitude waves and prevents the wave crest from sharpening in a self-similar manner. This raises many new questions about the behavior of large-amplitude standing waves, which we will explore in Section 4.4.

On the theoretical side, it has long been known [18, 19, 20] that standing water waves suffer from a small-divisor problem that obstructs convergence of the perturbation expansions developed by Rayleigh [21], Penney and Price [13], Tadjbakhsh and Keller [22], Concus [23], Schwartz and Whitney [1], and others. Penney and Price [13] went so far as to state, “there seems little likelihood that a proof of the existence of the stationary waves will ever be given.” Remarkably, Plotnikov and Toland [24], together with Iooss [20], have recently established existence of small-amplitude standing waves using a Nash-Moser iteration. As often happens in small-divisor problems [25, 26], solutions could only be proved to exist for values of an amplitude parameter in a totally disconnected Cantor set. No assertion is made about parameter values outside of this set. This raises intriguing new questions about whether resonance really causes a complete loss of smoothness in the dependence of solutions on amplitude, or if these results are an artifact of the use of Nash-Moser theory to prove existence. While a complete answer can only come through further analysis, insight can be gained by studying high precision numerical solutions.

In previous numerical studies, the most effective methods for computing standing water waves have been Fourier collocation in space and time [27, 5, 8, 28, 29], semi-analytic series expansions [1, 30], and shooting methods [2, 3, 7, 4]. In Fourier collocation, time-periodicity is built into the basis, and the equations of motion are imposed at collocation points to obtain a large nonlinear system of equations. This is the usual approach taken in analysis to prove existence of time-periodic solutions, e.g. of nonlinear wave equations [25] or nonlinear Schrödinger equations [26]. The drawback as a numerical method is that the number of unknowns in the nonlinear system grows like $(\Delta x \Delta t)^{-1}$ rather than Δx^{-1} for a shooting method, which limits the resolution one can achieve. Orthogonal collocation, as implemented in the software package AUTO [31], would be less efficient than Fourier collocation as more timesteps will be required to achieve the same accuracy.

The semi-analytic series expansions of Schwartz and Whitney [1, 30] are a significant improvement over previous perturbation methods [21, 13, 22, 23] in that the authors show how to compute an arbitrary number of terms rather than stopping at 3rd or 5th order. They also used conformal mapping to flatten the boundary, which leads to a more promising representation of the solution of Laplace’s equation. As a numerical method, the coefficients of the expansion are expensive to compute, which limits the number of terms one can obtain in practice. (Schwartz and Whitney stopped at 25th order). It may also be that the resulting series is an asymptotic series rather than a convergent series. Nevertheless, these series expansions play an essential role in the proof of existence of standing waves on deep water by Plotnikov, Toland and Iooss [20].

In a shooting method, one augments the known boundary values at one endpoint with additional prescribed data to make the initial value problem well posed, then looks for values of the new data to satisfy the boundary conditions at the other endpoint. For ordinary differential equations, this normally leads to a system of equations with the same number of equations as unknowns. The same is true of multi-shooting methods [32, 33, 34]. When the boundary value problem is governed by a system of partial differential equations, it is customary to discretize the PDE to obtain an ODE, then proceed as described above. However, because of aliasing errors, quadrature errors, filtering errors, and amplification by the derivative operator, discretization causes larger errors in high-frequency modes than low-frequency modes when the solution is evolved in time. These errors can cause the shooting method to be too aggressive in its search for initial conditions, and to explore regions of parameter space (the space of initial conditions) where either the numerical solution is inaccurate, or the physical solution becomes singular before reaching the other

endpoint. Even if safeguards are put in place to penalize high-frequency modes in the search for initial conditions, the Jacobian is often poorly conditioned due to these discretization errors.

We have found that posing boundary value problems governed by PDEs as overdetermined, nonlinear least squares problems can dramatically improve the robustness of shooting methods in two critical ways. First, we improve accuracy by padding the initial condition with high-frequency modes that are constrained to be zero. With enough padding, all the degrees of freedom controlled by the shooting method can be resolved sufficiently to compute a reliable Jacobian. Second, adding more rows to the Jacobian increases its smallest singular values, often improving the condition number by several orders of magnitude. The extra rows come from including the high-frequency modes of the boundary conditions in the system of equations, even though they are not included in the list of augmented initial conditions. As a rule of thumb, it is usually sufficient to set the top 1/3 to 1/2 of the Fourier spectrum to zero initially; additional zero-padding has little effect on the numerical solution or the condition number. Validation of accuracy by monitoring energy conservation and decay rates of Fourier modes will be discussed in Section 4.4, along with mesh refinement studies and comparison with quadruple precision calculations.

In this paper, we present two methods of solving the nonlinear least squares problem that arises in the overdetermined shooting framework. The first is the adjoint continuation method (ACM) of Ambrose and Wilkening [35, 36, 37, 38], in which the gradient of the objective function with respect to initial conditions is computed by solving an adjoint PDE, and the BFGS algorithm [39, 40] is used for the minimization. This was the approach used by one of the authors in her dissertation [41] to obtain the results of Sections 4.1 and 4.6. In the second approach, we exploit an opportunity for parallelism that makes computing the entire Jacobian feasible. Once this is done, a variant of the Levenberg-Marquardt method (with less frequent Jacobian updates) is used to rapidly converge to the solution. The main challenge here is organizing the computation to maximize re-use of setup costs in solving the variational equation with multiple right-hand sides, to minimize communication between threads or with the GPU device, and to ensure that most of the linear algebra occurs at level 3 BLAS speed. The performance of the algorithms on various platforms is reported in Section 4.7.

The scientific focus of the present work is on resonance and its effect on existence, non-uniqueness, and physical behavior of standing water waves. A summary of our main results is given in the abstract, and in more detail at the beginning of Section 4. We mention here that resonant modes generally take the form of higher-frequency, secondary standing waves oscillating at the surface of larger-scale, primary standing waves. Because the equations are nonlinear, only certain combinations of amplitude and phase can occur for each component wave. This leads to non-uniqueness through multiple branches of solutions. In shallow water, bifurcation curves of high-frequency Fourier modes behave erratically and contain many gaps where solutions do not appear to exist. This is expected on theoretical grounds. However, these bifurcation “curves” become smoother, or “heal,” as fluid depth increases. In infinite depth, such resonant effects are largely invisible, which we quantify and discuss in Section 5.

In future work [42], the methods of this paper will be used to study other families of time-periodic solutions of the free-surface Euler equations with less symmetry than is assumed here, e.g. traveling-standing waves, unidirectional solitary wave interactions, and collisions of gravity-capillary solitary waves. The stability of these solutions will also be analyzed in [42] using Floquet methods.

2. Equations of motion and time-stepping

The effectiveness of a shooting algorithm for solving two-point boundary value problems is limited by the accuracy of the time-stepper. In this section, we describe a boundary integral formulation of the water wave problem that is spectrally accurate in space and arbitrary order in time. We also describe how to implement the method in double and quadruple precision using a GPU, and discuss symmetries of the problem that can be exploited to reduce the work of computing standing waves by a factor of 4. The method is similar to other boundary integral formulations [43, 44, 45, 2, 3, 4, 46], but is simpler to implement than the angle–arclength formulation used in [47, 48, 49, 37], and avoids issues of identifying two curves that are equal “up to reparametrization” when the x and y coordinates of the interface are both evolved (in non-symmetric problems). Our approach also avoids sawtooth instabilities that sometimes occur when using Lagrangian markers [43, 2]. This is consistent with the results of Baker and Nachbin [50], who found that sawtooth instabilities can be controlled without filtering using the correct combination of spectral differentiation and interpolation schemes. While conformal mapping methods [51, 52, 53] are more efficient than boundary integral methods in many situations, they are not suitable for modeling extreme waves as the spacing between grid points expands severely in regions where wave crests form, which is the opposite of what is needed for an efficient representation of the solution via mesh refinement.

2.1. Equations of motion

We consider a two-dimensional irrotational ideal fluid [54, 55, 56, 57] bounded below by a flat wall and above by an evolving surface, $\eta(x, t)$. Because the flow is irrotational, there is a velocity potential ϕ such that $\mathbf{u} = \nabla\phi$. The restriction of ϕ to the free surface is denoted $\varphi(x, t) = \phi(x, \eta(x, t), t)$. The equations of motion governing $\eta(x, t)$ and $\varphi(x, t)$ are

$$\eta_t = \phi_y - \eta_x \phi_x, \quad (2.1a)$$

$$\varphi_t = P \left[\phi_y \eta_t - \frac{1}{2} \phi_x^2 - \frac{1}{2} \phi_y^2 - g\eta + \frac{\sigma}{\rho} \partial_x \left(\frac{\eta_x}{\sqrt{1 + \eta_x^2}} \right) \right]. \quad (2.1b)$$

Here g is the acceleration of gravity, ρ is the fluid density, $\sigma \geq 0$ is the surface tension (possibly zero), and P is the L^2 projection to zero mean that annihilates constant functions,

$$P = \text{id} - P_0, \quad P_0 f = \frac{1}{2\pi} \int_0^{2\pi} f(x) dx. \quad (2.2)$$

This projection is not standard in (2.1b), but yields a convenient convention for selecting the arbitrary additive constant in the potential. In fact, if the fluid has infinite depth and the mean surface height is zero, P has no effect in (2.1b) at the PDE level, ignoring roundoff and discretization errors. The velocity components $u = \phi_x$, $v = \phi_y$ on the right hand side of (2.1) are evaluated at the free surface to determine η_t and φ_t . The system is closed by relating ϕ in the fluid to η and φ on the surface as the solution of Laplace's equation

$$\phi_{xx} + \phi_{yy} = 0, \quad -h < y < \eta, \quad (2.3a)$$

$$\phi_y = 0, \quad y = -h, \quad (2.3b)$$

$$\phi = \varphi, \quad y = \eta, \quad (2.3c)$$

where h is the mean fluid depth (possibly infinite). We assume $\eta(x, t)$ and $\mathbf{u}(x, y, t)$ are 2π -periodic in x . Applying a horizontal Galilean transformation if necessary, we may also assume ϕ is 2π -periodic in x . We generally assume $h = 0$ in the finite depth case and absorb the mean fluid depth into η itself. This causes $-\eta(x)$ to be a reflection of the free surface across the bottom boundary, which simplifies many formulas in the boundary integral formulation below. The same strategy can also be applied in the presence of a more general bottom topography [52].

Equation (2.1a) is a kinematic condition requiring that particles on the surface remain there. Equation (2.1b) comes from $\varphi_t = \phi_y \eta_t + \phi_t$ and the unsteady Bernoulli equation, $\phi_t + \frac{1}{2} |\nabla\phi|^2 + gy + \frac{p}{\rho} = c(t)$, where $c(t)$ is constant in space but otherwise arbitrary. At the free surface, we assume the pressure jump across the interface due to surface tension is proportional to curvature, $p_0 - p|_{y=\eta} = \sigma\kappa$. The ambient pressure p_0 is absorbed into the arbitrary function $c(t)$, which is chosen to preserve the mean of $\varphi(x, t)$:

$$c(t) = \frac{p_0}{\rho} + P_0 \left[\eta_x \phi_x \phi_y + \frac{1}{2} \phi_x^2 - \frac{1}{2} \phi_y^2 + g\eta - \frac{\sigma}{\rho} \partial_x \left(\frac{\eta_x}{\sqrt{1 + \eta_x^2}} \right) \right]. \quad (2.4)$$

The advantage of this construction is that $\mathbf{u} = \nabla\phi$ is time-periodic with period T if and only if η and φ are time-periodic with the same period. Otherwise, $\varphi(x, T)$ could differ from $\varphi(x, 0)$ by a constant function without affecting the periodicity of \mathbf{u} .

Details of our boundary integral formulation are given in Appendix A. Briefly, we identify \mathbb{R}^2 with \mathbb{C} and parametrize the free surface by

$$\zeta(\alpha) = \xi(\alpha) + i\eta(\xi(\alpha)), \quad (2.5)$$

where the change of variables $x = \xi(\alpha)$ allows for smooth mesh refinement in regions of high curvature, and t has been suppressed in the notation. We compute the Dirichlet-Neumann operator [58],

$$\mathcal{G}\varphi(x) = \sqrt{1 + \eta'(x)^2} \frac{\partial\phi}{\partial n}(x + i\eta(x)), \quad (2.6)$$

which appears implicitly in the right hand side of (2.1) through ϕ_x and ϕ_y , in three steps. First, we solve the integral equation

$$\frac{1}{2}\mu(\alpha) + \frac{1}{2\pi} \int_0^{2\pi} [K_1(\alpha, \beta) + K_2(\alpha, \beta)]\mu(\beta) d\beta = \varphi(\xi(\alpha)) \quad (2.7)$$

for the dipole density, $\mu(\alpha)$, in terms of the (known) Dirichlet data $\varphi(\xi(\alpha))$. Formulas for K_1 and K_2 are given in (2.13) below. These kernels are smooth functions (even at $\alpha = \beta$), so the integral is not singular; see Appendix A. Second, we differentiate $\mu(\alpha)$ to obtain the vortex sheet strength, $\gamma(\alpha) = \mu'(\alpha)$. Finally, we evaluate the normal derivative of ϕ at the free surface via

$$\mathcal{G}\varphi(\xi(\alpha)) = \frac{1}{|\xi'(\alpha)|} \left[\frac{1}{2} H\gamma(\alpha) + \frac{1}{2\pi} \int_0^{2\pi} [G_1(\alpha, \beta) + G_2(\alpha, \beta)] \gamma(\beta) d\beta \right]. \quad (2.8)$$

G_1 and G_2 are defined in (2.13) below, and H is the Hilbert transform, which is diagonal in Fourier space with symbol $\hat{H}_k = -i \operatorname{sgn}(k)$. The only unbounded operation in this procedure is the second step, in which $\gamma(\alpha)$ is obtained from $\mu(\alpha)$ by taking a derivative.

Once $\mathcal{G}\varphi(x)$ is known, we compute ϕ_x and ϕ_y on the boundary using

$$\begin{pmatrix} \phi_x \\ \phi_y \end{pmatrix} = \frac{1}{1 + \eta'(x)^2} \begin{pmatrix} 1 & -\eta'(x) \\ \eta'(x) & 1 \end{pmatrix} \begin{pmatrix} \varphi'(x) \\ \mathcal{G}\varphi(x) \end{pmatrix}, \quad (2.9)$$

which allows us to evaluate (2.1a) and (2.1b) for η_t and φ_t . Alternatively, one can write the right hand side of (2.1) directly in terms of $\varphi'(x)$ and $\mathcal{G}\varphi(x)$.

2.2. GPU-accelerated time-stepping and quadruple precision

Next we turn to the question of discretization. Because we are interested in studying large amplitude standing waves that develop relatively sharp wave crests for brief periods of time, we discretize space and time adaptively. Time is divided into ν segments $\theta_l T$, where $\theta_1 + \dots + \theta_\nu = 1$ and T is the simulation time, usually an estimate of the period or quarter-period. In the simulations reported here, ν ranges from 1 to 5 and each θ_l was close to $1/\nu$ (within a factor of two). On segment l , we fix the number of (uniform) timesteps, N_l , the number of spatial grid points, M_l , and the function

$$\xi_l(\alpha) = \int_0^\alpha E_l(\beta) d\beta, \quad E_l(\alpha) = \begin{cases} 1 - P[A_l \sin^4(\alpha/2)], & \text{to refine near } x = \pi \\ 1 - P[A_l \cos^4(\alpha/2)], & \text{to refine near } x = 0 \end{cases}, \quad A_l = \frac{8(1 - \rho_l)}{5 + 3\rho_l}, \quad (2.10)$$

which controls the grid spacing in the change of variables $x = \xi_l(\alpha)$; see Figure 1. As before, P projects out the mean. The parameter ρ_l lies in the range $0 < \rho_l \leq 1$ and satisfies

$$\rho_l = \frac{\min\{E_l(0), E_l(\pi)\}}{\max\{E_l(0), E_l(\pi)\}}, \quad \min\{E_l(0), E_l(\pi)\} = \frac{8\rho_l}{5 + 3\rho_l}, \quad \max\{E_l(0), E_l(\pi)\} = \frac{8}{5 + 3\rho_l}. \quad (2.11)$$

Note that $\rho_l = 1$ corresponds to uniform spacing while $\rho_l = 0$ corresponds to the singular limit where ξ_l ceases to be a diffeomorphism at one point. This approach takes advantage of the fact that we can arrange in advance that the wave crests will form at $x = 0$ and $x = \pi$, alternating between the two in time. A more automated approach would be to have the grid spacing evolve with the wave profile, perhaps as a function of curvature, rather than asking the user to specify the change of variables. We did not experiment with this idea since our approach also allows the number of

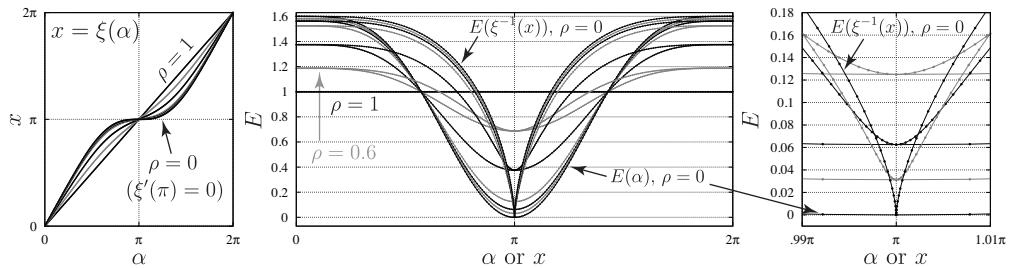


Figure 1: Dependence of mesh spacing on the parameter ρ (dropping the subscript l) in (2.10), with mesh refinement near $x = \pi$. (left) Plots of $x = \xi(\alpha)$ for $\rho = 0.0, 0.02, 0.04, 0.08, 0.25, 0.6$ and 1.0 . (center) $E(\alpha) = \partial\xi/\partial\alpha$ represents the grid spacing relative to uniform spacing. Comparison of $E(\alpha)$ and $E(\xi^{-1}(x))$ shows how the grid points are re-distributed. (right) A magnified view near $\alpha = \pi$ shows that when ρ reaches 0, $\xi(\alpha)$ ceases to be a diffeomorphism and $E(\xi^{-1}(x))$ forms a cusp.

grid points to increase in time, which would be complicated in an automated approach. We always set $\rho_1 = 1$ so that $x = \alpha$ on the first segment. Respacing the grid from segment l to $l + 1$ boils down to interpolating η and φ to obtain values on the new mesh, e.g. $\eta \circ \xi_{l+1}(\alpha_j) = \eta \circ \xi_l(\xi_l^{-1} \circ \xi_{l+1}(\alpha_j))$, $\alpha_j = 2\pi j/M_l$, which is straightforward by Newton's method. To be safe, we avoid refining the mesh in one region at the expense of another; thus, if $\rho_{l+1} < \rho_l$, we also require $(M_{l+1}/M_l) \geq (5 + 3\rho_l)/(5 + 3\rho_{l+1})$ so that the grid spacing decreases throughout the interval, but more so in the region where the wave crest is forming.

Since the evolution equations are not stiff unless the surface tension is large, high order explicit time-stepping schemes work well. For each Runge-Kutta stage within a timestep on a given segment l , the integral equation (2.7) is solved by collocation using uniformly spaced grid points $\alpha_j = 2\pi j/M_l$ and the (spectrally accurate) trapezoidal rule,

$$\frac{1}{2\pi} \int_0^{2\pi} K(\alpha_i, \beta) \mu(\beta) d\beta \approx \frac{1}{M_l} \sum_{j=0}^{M_l-1} K(\alpha_i, \alpha_j) \mu(\alpha_j). \quad (2.12)$$

The matrices $K_{ij} = K(\alpha_i, \alpha_j)/M_l$ and $G_{ij} = G(\alpha_i, \alpha_j)/M_l$ that represent the discretized integral operators in (2.7) and (2.8) are computed simultaneously and in parallel. The formulas are $K(\alpha, \beta) = K_1(\alpha, \beta) + K_2(\alpha, \beta)$ and $G(\alpha, \beta) = G_1(\alpha, \beta) + G_2(\alpha, \beta)$ with

$$\begin{aligned} K_1 &= \text{Im} \left\{ \frac{\zeta'(\beta)}{2} \cot \frac{\zeta(\alpha) - \zeta(\beta)}{2} - \frac{1}{2} \cot \frac{\alpha - \beta}{2} \right\}, & K_2 &= \text{Im} \left\{ \frac{\bar{\zeta}'(\beta)}{2} \cot \frac{\zeta(\alpha) - \bar{\zeta}(\beta)}{2} \right\}, \\ G_1 &= \text{Re} \left\{ \frac{\zeta'(\alpha)}{2} \cot \frac{\zeta(\alpha) - \zeta(\beta)}{2} - \frac{1}{2} \cot \frac{\alpha - \beta}{2} \right\}, & G_2 &= \text{Re} \left\{ \frac{\zeta'(\alpha)}{2} \cot \frac{\zeta(\alpha) - \bar{\zeta}(\beta)}{2} \right\}. \end{aligned} \quad (2.13)$$

As explained in Appendix A, these kernels have been regularized. Indeed, $K_1(\alpha, \beta)$ and $G_1(\alpha, \beta)$ are continuous at $\beta = \alpha$ if we define $K_1 = -\text{Im}\{\zeta''(\alpha)/[2\zeta'(\alpha)]\}$ and $G_1 = \text{Re}\{\zeta''(\alpha)/[2\zeta'(\alpha)]\}$. These formulas are used when computing the diagonal entries K_{ii} and G_{ii} . The terms $\cot((\alpha - \alpha_j)/2)$ in (2.13) are computed once and for all at the start. If the fluid depth is infinite, K_2 and G_2 are omitted. GMRES is used to solve (2.7) for μ , which consistently takes 4-30 iterations to reach machine precision (independent of problem size). In quadruple precision, the typical range is 9-36 GMRES iterations. The FFT is used to compute μ' and $H\gamma$ in (2.8), as well as ζ' , ζ'' , η' , and φ' .

We wrote 3 versions of the code, which differ only in how the matrices K and G are computed. The simplest version uses openMP *parallel for* loops to distribute the work among all available threads. The most complicated version is parallelized using MPI and scalapack. In this case, the matrices K and G are stored in block-cyclic layout [59] across the processors, and each processor computes only the matrix entries it is responsible for. The fastest version of the code is parallelized on a GPU in the cuda programming language. First, the CPU sends the GPU the vector $\zeta(\alpha_j)$, which holds M_l complex numbers. Next, the GPU computes the matrices K and G and stores them in device memory. Finally, in the GMRES iteration, Krylov vectors are sent to the GPU, which applies the matrix K and returns the result as a vector. After the last Krylov iteration, the device also applies G to μ to help compute $\mathcal{G}\varphi$ in (2.8). Thus, communication with the GPU involves passing vectors of length M_l , while $O(M_l^2)$ flops must be performed on each vector passed in. As a result, communication does not pose a computational bottleneck, and the device operates at near 100% efficiency. We remark that the formula

$$\cot \frac{x + iy}{2} = \begin{cases} [\cos(x) + \cosh(y)]/[\sin(x) + i \sinh(y)], & \cos(x) \geq 0, \\ [\sin(x) - i \sinh(y)]/[\cosh(y) - \cos(x)], & \cos(x) < 0 \end{cases}$$

is relatively expensive to evaluate. Thus, it pays to compute K and G simultaneously (to re-use \sin , \cos , \sinh , \cosh results), and to actually store the matrices in device memory rather than re-compute the matrix entries each time a matrix-vector product is required.

In double-precision, we evolve (2.1) using Dormand and Prince's DOP853 scheme [60]. This is a 13 stage, 8th order, "first same as last" Runge-Kutta method, so the effective cost of each step is 12 function evaluations. We apply the 36th order filter described in [61] to the right hand side of (1e) and (1f) each time they are evaluated in the Runge-Kutta procedure, and to the solution itself at the end of each time-step. This filter consists of multiplying the k th Fourier mode by

$$\exp[-36(|k|/k_{\max})^{36}], \quad k_{\max} = M/2, \quad (2.14)$$

which allows the highest-frequency Fourier modes to remain non-zero (to help resolve the solution) while still suppressing aliasing errors. To achieve truncation errors of order 10^{-30} in quadruple-precision, the 8th order method

requires too many timesteps. Through trial and error, we found that a 15th order spectral deferred correction (SDC) method [62, 63, 64] is the most efficient scheme for achieving this level of accuracy. Our GPU implementation of quadruple precision arithmetic will be discussed briefly in Section 3.3. The variant of SDC that we use in this paper employs eight Radau IIA quadrature nodes [60]. The initial values at the nodes are obtained via fourth order Runge-Kutta. Ten correction sweeps are then performed to improve the solution to $O(h^{15})$ accuracy at the quadrature nodes. We use pure Picard corrections instead of the more standard forward-Euler corrections as they have slightly better stability properties. The final integration step yields a local truncation error of $O(h^{16})$; hence, the method is 15th order. See [65] for more information about this variant of the SDC method and its properties. If one wished to go beyond quadruple-precision arithmetic, it is straightforward to increase the order of the time-stepping scheme accordingly. We did not investigate the use of symplectic integrators since our approach already conserves energy to 12-16 digits of accuracy in double precision, and 24-32 digits in quadruple precision.

2.3. Translational and time-reversal symmetry

In this paper, we restrict attention to symmetric standing waves of the type studied in [21, 13, 22, 23, 2, 3, 7, 28]. For these waves, it is only necessary to evolve the solution over a quarter period. Indeed, if at some time $T/4$ the fluid comes to rest ($\varphi \equiv 0$), a time-reversal argument shows that the solution will evolve back to the initial state at $T/2$ with the sign of φ reversed. More precisely, the condition $\varphi(x, T/4) = 0$ implies that $\eta(x, T/2) = \eta(x, 0)$ and $\varphi(x, T/2) = -\varphi(x, 0)$. Now suppose that, upon translation by π , $\eta(x, 0)$ remains invariant while $\varphi(x, 0)$ changes sign. Then we see that $\eta_1(x, t) = \eta(x + \pi, T/2 + t)$ and $\varphi_1(x, t) = \varphi(x + \pi, T/2 + t)$ are solutions of (2.1) with initial conditions

$$\begin{aligned}\eta_1(x, 0) &= \eta(x + \pi, T/2) = \eta(x + \pi, 0) = \eta(x, 0), \\ \varphi_1(x, 0) &= \varphi(x + \pi, T/2) = -\varphi(x + \pi, 0) = \varphi(x, 0).\end{aligned}$$

Therefore, $\eta_1 = \eta$, $\varphi_1 = \varphi$, and

$$\begin{aligned}\eta(x, T) &= \eta_1(x - \pi, T/2) = \eta(x - \pi, T/2) = \eta(x - \pi, 0) = \eta(x, 0), \\ \varphi(x, T) &= \varphi_1(x - \pi, T/2) = \varphi(x - \pi, T/2) = -\varphi(x - \pi, 0) = \varphi(x, 0).\end{aligned}$$

Hence, η and φ are time-periodic with period T . It is natural to expect standing waves to have even symmetry when the origin is placed at a crest or trough and the fluid comes to rest. This assumption implies that η and φ will remain even functions for all time since η_t and φ_t in (2.1) are even whenever η and φ are. Under all these assumptions, the evolution of η and φ from $T/2$ to T is a mirror image (about $x = \frac{\pi}{2}$ or $x = \frac{3\pi}{2}$) of the evolution from 0 to $T/2$.

Once the initial conditions and period are found using symmetry to accelerate the search for time-periodic solutions, we double-check that the numerical solution evolved from 0 to T is indeed time-periodic. Mercer and Roberts exploited similar symmetries in their numerical computations [2, 3].

3. Overdetermined shooting methods

As discussed in the introduction, two-point boundary value problems governed by partial differential equations must be discretized before solving them numerically. However, truncation errors lead to loss of accuracy in the highest-frequency modes of the numerical solution, which can cause difficulty for the convergence of shooting methods. We will see below that robustness can be achieved by posing these problems as overdetermined nonlinear systems.

In Section 3.1, we define two objective functions with the property that driving them to zero is equivalent to finding a time-periodic standing wave. One of the objective functions exploits the symmetry discussed above to reduce the simulation time by a factor of 4. The other is more robust as it naturally penalizes high-frequency Fourier modes of the initial conditions. Both objective functions use symmetry to reduce the number of unknowns and eliminate phase shifts of the standing waves in space and time. The problem is overdetermined because the highest-frequency Fourier modes are constrained to be zero initially but not at the final time. Also, because $T/4$ often corresponds to a sharply crested wave profile, there are more active Fourier modes in the solution at that time than at $t = 0$. By refining the mesh adaptively, we include all of these active modes in the objective functions, making them more overdetermined. The idea that the underlying dynamics of standing water waves is lower-dimensional than predicted by counting active Fourier modes has recently been explored by Williams, *et al.* [66].

In Sections 3.2 and 3.3, we describe two methods for solving the resulting nonlinear least squares problem. The first is the Adjoint Continuation Method [35, 36, 37, 38], in which the gradient of the objective function is computed

by solving an adjoint PDE and the BFGS algorithm [39, 40] is used for the minimization. The second is a trust-region approach in which the Jacobian is computed by solving the variational equation in parallel with multiple right-hand sides. This allows the work of computing the Dirichlet-Neumann operator to be shared across all the columns of the Jacobian. We also discuss implementation issues in quadruple precision on a GPU.

3.1. Nonlinear least squares formulation

In the symmetric standing wave case considered here, we assume the initial conditions are even functions satisfying $\eta(x + \pi, 0) = \eta(x, 0)$ and $\varphi(x + \pi, 0) = -\varphi(x, 0)$. In Fourier space, they take the form

$$\begin{aligned}\hat{\eta}_k(0) &= c_{|k|}, & (k = \pm 2, \pm 4, \pm 6, \dots ; |k| \leq n), \\ \hat{\varphi}_k(0) &= c_{|k|}, & (k = \pm 1, \pm 3, \pm 5, \dots ; |k| \leq n),\end{aligned}\tag{3.15}$$

where c_1, \dots, c_n are real numbers, and all other Fourier modes of the initial conditions are set to zero. (In the finite depth case, we also set $\hat{\eta}_0 = h$, the mean fluid depth.) Here n is taken to be somewhat smaller than M_1 , e.g. $n \approx \frac{1}{3}M_1$, where M_1 is the number of spatial grid points used during the first N_1 timesteps. (Recall that subscripts on M and N refer to mesh refinement sub-intervals.) Note that high-frequency Fourier modes of the initial condition are zero-padded to improve resolution of the first n Fourier modes.

In addition to the Fourier modes of the initial condition, the period of the solution is unknown. We add a zeroth component to c to represent the period:

$$T = c_0.\tag{3.16}$$

Our goal is to find $c \in \mathbb{R}^{n+1}$ such that $\varphi(x, T/4) = 0$. We therefore define the objective function

$$f(c) = \frac{1}{2}r(c)^T r(c) \approx \frac{1}{4\pi} \int_0^{2\pi} \varphi(x, T/4)^2 dx, \quad r_i = \varphi(\xi_\nu(\alpha_i), T/4) \sqrt{E_\nu(\alpha_i)/M_\nu},\tag{3.17}$$

where ν is the index of the final sub-interval in the mesh refinement strategy and the square root is a quadrature weight to approximate the integral via the trapezoidal rule after the change of variables $x = \xi_\nu(\alpha)$, $dx = E_\nu(\alpha) d\alpha$. Note that $r \in \mathbb{R}^m$ with $m = M_\nu$, which is usually several times larger than n , the number of non-zero initial conditions. The numerical solution is not sensitive to the choice of m and n as long as enough zero-padding is included in the initial condition to resolve the highest frequency Fourier modes. This will be confirmed in Section 4.4 through mesh-refinement studies and comparison with quadruple-precision computations.

One can also use an objective function that measures deviation from time-periodicity directly:

$$f(c) \approx \frac{1}{4\pi} \int_0^{2\pi} [\eta(x, T) - \eta(x, 0)]^2 + [\varphi(x, T) - \varphi(x, 0)]^2 dx.\tag{3.18}$$

When the underlying PDE is stiff (e.g. for the Benjamin-Ono [35, 36] or KdV equations), an objective function of the form (3.18) has a key advantage over (3.17). For stiff problems, semi-implicit time-stepping methods are used in order to take reasonably large time-steps. Such methods damp high-frequency modes of the initial condition. This causes these modes to have little effect on an objective function of the form (3.17); thus, the Jacobian $J_{ij} = \partial r_i / \partial c_j$ can be poorly conditioned if the shooting method attempts to solve for too many modes. By contrast, when implemented via (3.18), the initial conditions of high-frequency modes are heavily penalized for deviating from the damped values at time T . As a result, the Jacobian does not suffer from rank deficiency, and high-frequency modes do not drift far from zero unless doing so is helpful. Since the water wave is not stiff, we use explicit schemes that do not significantly damp high-frequency modes; therefore, the computational advantage of evolving over a quarter-period outweigh any robustness advantage of using (3.18).

We used symmetry to reduce the number of unknown initial conditions in (3.15). This has the added benefit of selecting the spatial and temporal phase of each solution in a systematic manner. In problems where the symmetries of the solution are not known in advance, or to search for symmetry-breaking bifurcations, one can revert to the approach described in [35], where both real and imaginary parts of the leading Fourier modes of the initial condition were computed in the search for time-periodic solutions. To eliminate spatial and temporal phase shifts, one of the Fourier modes was constrained to be real and its time derivative was required to be imaginary. Constraining the time-derivative of a mode is most easily done with a penalty function [35]. Alternatively, if two modes are constrained to be real and their time-derivatives are left arbitrary, it is easier to remove their imaginary parts from the search space than to use a penalty function.

Once phase shifts have been eliminated, the families of time-periodic solutions we have found appear to sweep out two-parameter families of solutions. To compute a solution in a family, we specify the mean depth and the value of one of the c_k in (3.15) or (3.16) and solve for the other c_j to minimize the objective function. If f is reduced below a specified threshold (typically 10^{-26} in double-precision or 10^{-52} in quadruple precision), we consider the solution to be time-periodic. If f reaches a local minimum that is higher than the specified threshold, we either (1) refine the mesh, increase n , and try again; (2) choose a different value of c_k closer to the previous successful value; or (3) change the index k specifying which Fourier mode is used as a bifurcation parameter. Switching to a different k is often useful when tracking a fold in the bifurcation curve. Since $c \in \mathbb{R}^{n+1}$ and one parameter has been frozen, f is effectively a function of n variables.

We note that once n and the mesh parameters ν , θ_l , A_l , M_l and N_l are chosen, $f(c)$ is a smooth function that can be minimized using a variety of optimization techniques. Small divisors come into play when deciding whether f would really converge to zero in the mesh refinement limit (with ever increasing numerical precision). The answer may depend on whether the bifurcation parameters ($\hat{\eta}_0$ and either $\eta(a, 0)$ or one of the c_k) are allowed to vary within the tolerance of the current roundoff threshold each time the mesh is refined and the floating point precision is increased. While it is likely that small divisors prevent the existence of smooth families of exact solutions, exceedingly accurate approximate solutions do appear to sweep out smooth families, with occasional disconnections in the bifurcation curves due to resonance.

3.2. Adjoint continuation method

Having recast the shooting method as an overdetermined nonlinear least squares problem, we must now minimize the functional f in (3.17) or (3.18). The first approach we tried was the adjoint continuation method (ACM) developed by Ambrose and Wilkening to study time-periodic solutions of the Benjamin-Ono equation [35, 36] and the vortex sheet with surface tension [37]. The method has also been used by Williams *et al.* to study the stability transition from single-pulse to multi-pulse dynamics in a mode-locked laser system [38].

The idea of the ACM is to compute the gradient of f with respect to the initial conditions by solving an adjoint PDE, and then minimize f using the BFGS method [39, 40]. BFGS is a quasi-Newton algorithm that builds an approximate (inverse) Hessian matrix from the sequence of gradient vectors it encounters on successive line-searches. In more detail, let $q = (\eta, \varphi)$ and denote the system (2.1) abstractly by

$$q_t = F(q), \quad q(x, 0) = q_0(x). \quad (3.19)$$

We define the inner product

$$\langle q_1, q_2 \rangle = \frac{1}{2\pi} \int_0^{2\pi} [\eta_1(x)\eta_2(x) + \varphi_1(x)\varphi_2(x)] dx \quad (3.20)$$

so that f in (3.17), written now as a function of the initial conditions and proposed period, which themselves depend on c via (3.15) and (3.16), takes the form

$$f(q_0, T) = \frac{1}{2} \|(0, \varphi(\cdot, T/4))\|^2 = \frac{1}{4\pi} \int_0^{2\pi} \varphi(x, T/4)^2 dx, \quad (3.21)$$

where $q = (\eta, \varphi)$ solves (3.19). The case with f of the form (3.18) is similar, so we omit details here. In the course of minimizing f , the BFGS algorithm will repeatedly query the user to evaluate both $f(c)$ and its gradient $\nabla_c f(c)$ at a sequence of points $c \in \mathbb{R}^{n+1}$. The T derivative, $\partial f / \partial c_0$, is easily obtained by evaluating

$$\frac{\partial f}{\partial T} = \frac{1}{8\pi} \int_0^{2\pi} \varphi(x, T/4) \varphi_t(x, T/4) dx \quad (3.22)$$

using the trapezoidal rule after changing variables, $x = \xi_v(\alpha)$, $dx = E_v(\alpha) d\alpha$. Note that $\varphi(\cdot, T/4)$ and $\varphi_t(\cdot, T/4)$ are already known by solving (2.1). One way to compute the other components of $\nabla_c f$, say $\partial f / \partial c_k$, would be to solve the variational equation, (written abstractly here and explicitly in Appendix B)

$$\dot{q}_t = DF(q(\cdot, t))\dot{q}, \quad \dot{q}(x, 0) = \dot{q}_0(x) \quad (3.23)$$

with initial conditions

$$\dot{q}_0(x) = \begin{cases} (e^{ikx} + e^{-ikx}, 0), & k = 1, 3, 5, \dots \\ (0, e^{ikx} + e^{-ikx}), & k = 2, 4, 6, \dots \end{cases} \quad (3.24)$$

to obtain

$$\frac{\partial f}{\partial c_k} = \dot{f} = \left. \frac{d}{d\varepsilon} \right|_{\varepsilon=0} f(q_0 + \varepsilon \dot{q}_0, T) = \langle (0, \varphi(\cdot, T/4)), (0, \dot{\varphi}(\cdot, T/4)) \rangle. \quad (3.25)$$

Note that a dot denotes a directional derivative with respect to the initial condition, not a time-derivative. To avoid the expense of solving (3.23) repeatedly for each value of k , we solve a single adjoint PDE to find $\delta f / \delta q_0$ such that $\dot{f} = \langle \delta f / \delta q_0, \dot{q}_0 \rangle$. From (3.25), we have

$$\dot{f} = \langle (0, \varphi(\cdot, T/4)), (\dot{\eta}(\cdot, T/4), \dot{\varphi}(\cdot, T/4)) \rangle = \langle \tilde{q}_0, \dot{q}(\cdot, T/4) \rangle, \quad (3.26)$$

where we have defined $\tilde{q}_0 = (\tilde{\eta}_0, \tilde{\varphi}_0)$ with $\tilde{\eta}_0 = 0$ and $\tilde{\varphi}_0 = \varphi(\cdot, T/4)$. Note that replacing 0 by $\dot{\eta}(\cdot, T/4)$ did not affect the inner product. Next we observe that the solution $\tilde{q}(x, s)$ of the adjoint equation

$$\tilde{q}_s = DF(q(\cdot, T/4 - s))^* \tilde{q}, \quad \tilde{q}(\cdot, 0) = \tilde{q}_0, \quad (3.27)$$

which evolves backward in time ($s = T/4 - t$), has the property that

$$\langle \tilde{q}(\cdot, T/4 - t), \dot{q}(\cdot, t) \rangle = \text{const}. \quad (3.28)$$

Setting $t = T/4$ shows that this constant is actually \dot{f} . Setting $t = 0$ gives the form we want:

$$\dot{f} = \langle \delta f / \delta q_0, \dot{q}_0 \rangle, \quad \frac{\delta f}{\delta q_0} = \tilde{q}(\cdot, T/4). \quad (3.29)$$

From (3.24), we obtain

$$\frac{\partial f}{\partial c_k} = \begin{cases} 2 \operatorname{Re} \{ \tilde{\eta}_k^\wedge(T/4) \}, & k = 1, 3, 5, \dots \\ 2 \operatorname{Re} \{ \tilde{\varphi}_k^\wedge(T/4) \}, & k = 2, 4, 6, \dots \end{cases}. \quad (3.30)$$

Together with (3.22), this gives all the components of $\nabla_c f$ at once. Explicit formulas for the linearized and adjoint equations (3.23) and (3.27) are derived in Appendix B.

Like (3.23), the adjoint equation (3.27) is linear, but non-autonomous, due to the presence of the solution $q(t)$ of (3.19) in the equation. In the BFGS method, the gradient is always called immediately after computing the function value; thus, if $q(t)$ and $q_t(t)$ are stored in memory at each timestep in the forward solve, they are available in the adjoint solve at intermediate Runge-Kutta steps through cubic Hermite interpolation. We actually use dense output formulas [67, 60] for the 5th and 8th order Dormand-Prince schemes since cubic Hermite interpolation limits the accuracy of the adjoint solve to 4th order, but the idea is the same. If there is insufficient memory to store the solution at every timestep, we store the solution at equally spaced mile-markers and re-compute q between them when \tilde{q} reaches that region. Thus, ∇f can be computed in approximately the same amount of time as f itself, or twice the time if mile-markers are used.

It is worth mentioning that, when discretized, the values of η and φ are stored on a non-uniformly spaced grid for each segment $l \in \{2, \dots, \nu\}$ in the mesh-refinement strategy. The adjoint variables $\tilde{\eta}$, $\tilde{\varphi}$ are stored at the same mesh points, and are initialized by

$$\tilde{\eta}_0 \circ \xi_\nu(\alpha_i) = 0, \quad \tilde{\varphi}_0 \circ \xi_\nu(\alpha_i) = \varphi(\xi_\nu(\alpha_i), T/4),$$

with no additional weight factors needed. This works because the inner product (3.20) is defined with respect to x rather than α , and the change of variables has been accounted for by the factor $\sqrt{E_\nu(\alpha_i)/M_\nu}$ in the formula (3.17) for f .

3.3. Trust-region shooting method

While the ACM method gives an efficient way of computing the gradient of f , it takes many line-search iterations to build up an accurate approximation of the Hessian of f . This misses a key opportunity for parallelism and re-use of data that can be exploited if we switch from the BFGS framework to a Levenberg-Marquardt approach [40]. Instead of solving the adjoint equation (3.27) to compute ∇f efficiently, we solve the variational equation (3.23) with multiple right-hand sides to compute all the columns of the Jacobian simultaneously. From (3.17), we see that

$$J_{ik} = \frac{\partial r_i}{\partial c_k} = \begin{cases} \varphi_i(\xi_\nu(\alpha_i), T/4) \sqrt{E_\nu(\alpha_i)/M_\nu}, & k = 0, \\ \dot{\varphi}_i(\xi_\nu(\alpha_i), T/4) \sqrt{E_\nu(\alpha_i)/M_\nu}, & k \geq 1, \end{cases} \quad (3.31)$$

where \dot{q}_0 is initialized as in (3.24) for $k \geq 1$. We avoid the need to store q at every timestep (or at mile-markers) by evolving q along with \dot{q} rather than interpolating q :

$$\frac{\partial}{\partial t} \begin{pmatrix} q \\ \dot{q} \end{pmatrix} = \begin{pmatrix} F(q) \\ DF(q)\dot{q} \end{pmatrix}, \quad \begin{aligned} q(0) &= q_0 = (\eta_0, \varphi_0), \\ \dot{q}(0) &= \dot{q}_0 = \partial q_0 / \partial c_k. \end{aligned} \quad (3.32)$$

In practice, we replace \dot{q} in (3.32) by the matrix $\dot{Q} = [\dot{q}_{(k=1)}, \dots, \dot{q}_{(k=n)}]$ to compute all the columns of J (besides $k = 0$) at once. The linearized equations (B.1) involve the same Dirichlet-to-Neumann operator as the nonlinear equations (2.1), so the matrices K and G in (2.7) and (2.8) only have to be computed once to evolve the entire matrix \dot{Q} through a Runge-Kutta stage. Moreover, the linear algebra involved can be implemented at level 3 BLAS speed. For large problems, we perform an LU-factorization of K , the cost of which is made up for many times over by replacing GMRES iterations with a single back-solve stage for each right-hand side. In the GPU version of the code, all the linear algebra involving K and G is performed on the device (using the CULA library). As before, communication with the device is minimal in comparison to the computational work performed there.

We emphasize that the main advantage of solving linearized equations is that the same DNO operator is used for each column of \dot{Q} in a given Runge-Kutta stage. This opportunity is lost in the simpler approach of approximating J through finite differences by evolving (3.19) repeatedly, with initial conditions perturbed in each coordinate direction:

$$J_{ik} \approx \frac{r_i(c + \varepsilon e_k) - r_i(c)}{\varepsilon}, \quad e_k = (0, \dots, 0, 1, 0, \dots, 0)^T \in \mathbb{R}^{n+1}. \quad (3.33)$$

Thus, while finite differences can also be parallelized efficiently by evolving these solutions independently, the matrices K and G will be computed n times more often in the finite difference approach, and most of the linear algebra will drop from running at level 3 BLAS speed to level 2. Details of our Levenberg-Marquardt implementation are given in Appendix C, where we discuss how to re-use the Jacobian several times rather than re-computing it each time a step is accepted.

The CULA and LAPACK libraries could not be used for quadruple precision calculations, and we did not try FFTW in that mode. Instead, we used custom FFT and linear algebra libraries (written by Wilkening) for this purpose. However, for the GPU, we did not have any previous code to build on. Our solution was to write a block version of matrix-matrix multiplication in CUDA to compute residuals in quadruple precision, then use iterative refinement to solve for the corrections in double-precision, using the CULA library. Although quadruple precision is not native on any current GPU, we found M. Lu's *gqd* package [68], which is a CUDA implementation of Bailey's *qd* package [69], to be quite fast. Our code is written so that the floating point type can be changed through a simple *typedef* in a header file. This is possible in C++ by overloading function names and operators to call the appropriate versions of routines based on the argument types.

4. Numerical results

This section is organized as follows: In Section 4.1, we use the Adjoint Continuation Method to study standing waves of wavelength 2π in water of uniform depth $h = 1$. Several disconnections in the bifurcation curves are encountered, which are shown to correspond physically to higher-frequency standing waves superposed (nonlinearly) on the low-frequency carrier wave. In Section 4.2, we use the trust-region approach to study a nucleation event in which isolated large-amplitude solutions, and closed loops of such solutions, suddenly exist for depths below a threshold value. This gives a new mechanism for the creation of additional branches of solutions (besides harmonic resonance [3, 4]). In Section 4.3, we study a ‘‘Wilton ripple’’ phenomenon [70, 71, 6, 72, 73] in which a pair of ‘‘mixed mode’’ solutions bifurcate along side the ‘‘pure mode’’ solutions at a critical depth. Our numerical solutions are accurate enough to identify the leading terms in the asymptotic expansion of these mixed mode solutions. Following the mixed-mode branches via numerical continuation reveals that they meet up with the pure mode branches again at large amplitude. We also study how this degenerate bifurcation splits when the fluid depth is perturbed. In Section 4.4, we study what goes wrong in the Penney and Price conjecture, which predicts that the limiting standing wave of extreme form will develop sharp 90 degree corner angles at the wave crests. We also discuss energy conservation, decay of Fourier modes, and validation of accuracy. In Section 4.5, we study collisions of counter-propagating solitary water waves that are elastic in the sense that the background radiation is identical before and after the collision. In Section 4.6, we study time-periodic gravity-capillary waves of the type studied by Concus [23] and Vanden-Broeck [70] using perturbation theory. Finally, in Section 4.7, we compare the performance of the algorithms on a variety of parallel machines, using MINPACK as a benchmark for solving nonlinear least squares problems.

4.1. Standing waves of unit depth

We begin by computing a family of symmetric standing waves with mean fluid depth $\hat{\eta}_0 = h = 1$ and zero surface tension. The linearized equations about a flat rest state are

$$\dot{\eta}_t = \mathcal{G}\dot{\varphi}, \quad \dot{\varphi}_t = P[-g\dot{\eta}], \quad (\mathcal{G}[e^{ikx}] = [k \tanh kh]e^{ikx}). \quad (4.34)$$

Thus, the linearized problem has standing wave solutions of the form

$$\dot{\eta} = A \sin \omega t \cos kx, \quad \dot{\varphi} = B \cos \omega t \cos kx, \quad \omega^2 = kg \tanh kh, \quad A/B = \sqrt{(k/g) \tanh kh}. \quad (4.35)$$

Setting $h = 1, g = 1, k = 1$, these solutions have period $T = 2\pi/\omega \approx 7.19976$. Here B is a free parameter controlling the amplitude, and A is determined by $A/B = \sqrt{\tanh 1}$.

To find time-periodic solutions of the nonlinear problem, we start with a small amplitude linearized solution as an initial guess. Holding $c_1 = \hat{\varphi}_1(0)$ constant, we solve for the other c_k in (3.15) using the ACM method of Section 3.2. Note that $c_1 = B$ in the linearized regime. We then repeat this procedure for another value of c_1 to obtain a second small-amplitude solution of the nonlinear problem. The particular choices we made were $c_1 = -0.001$ and $c_1 = -0.002$. We then varied c_1 in increments of -0.001 , using linear extrapolation from the previous two solutions for the initial guess. The results are shown in Fig. 2. The two representative solutions labeled A and B show that the amplitude of the wave increases and the crest sharpens as the magnitude of c_1 increases. We chose c_1 to be negative so the peak at $T/4$ would occur at $x = \pi$ rather than $x = 0$. An identical bifurcation curve (reflected about the T -axis) would be obtained by increasing c_1 from 0 to positive values. The solutions A and B would then be shifted by π in space.

For most values of c_1 between 0.0 and -0.23 , the ACM method has no difficulty finding time-periodic solutions to an accuracy of $f < 10^{-26}$. However, at $c_1 = -0.201$, the minimum value of f exceeds this target. On further investigation, we found there was a small gap, $c_1 \in (-0.20113, -0.20124)$, where we were unable to compute time-periodic solutions even after increasing M from 256 to 512 and decreasing the continuation stepsize to $\Delta c_1 = 1.0 \times 10^{-5}$. By plotting other Fourier modes of the initial conditions versus the period, we noticed that the 9th mode jumps discontinuously when c_1 crosses this gap. A similar disconnection appears to be developing near solution B.

Studying the results of Fig. 2, we suspected we could find additional solutions by back-tracking from B to the region of the bifurcation curve around $c_9 = -7.0 \times 10^{-6}$ and performing a large extrapolation step to $c_9 \approx -1.0 \times 10^{-5}$, hoping to jump over the disconnection at B. This worked as expected, causing us to land on the branch that terminates at G in Fig 3. We used the same technique to jump from this branch to a solution between E and D. We were unable to find any new branches beyond C by extrapolation from earlier consecutive pairs of solutions.

Next we track each solution branch as far as possible in each direction. This requires switching among the c_k as bifurcation parameters when traversing different regions of the solution space. The period, $c_0 = T$, is one of the options. We also experimented with pseudo-arclength continuation [32, 31, 4], but found that it is necessary to rescale the Fourier modes to successfully traverse folds in the bifurcation diagram. This requires just as much human intervention as switching among the c_k , so we abandoned the approach. The disconnections at A and B turn out to meet each other, so that B is part of a closed loop and A is connected to the branch containing G. We stopped at G, F, C because the computations became too expensive to continue further with the desired accuracy of $f < 10^{-26}$ using the adjoint continuation method.

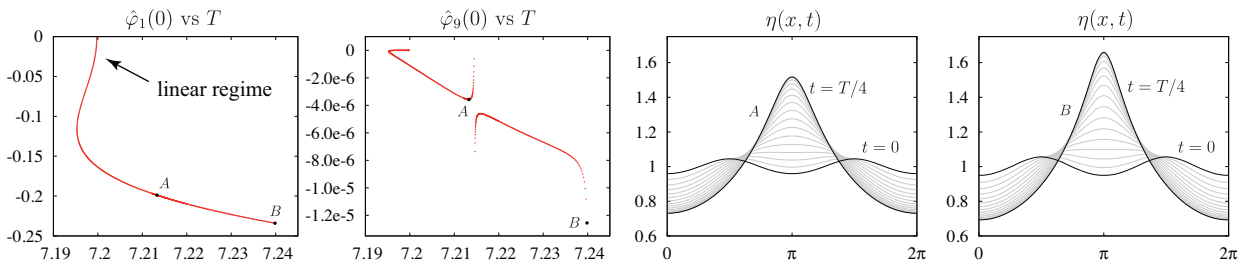


Figure 2: A family of standing water waves of unit depth ($h = 1$) bifurcates from the stationary solution at $T = 2\pi/\sqrt{\tanh 1} \approx 7.200$. We used the ACM method to track the family out of the linearized regime via numerical continuation. The period initially decreases with amplitude, but later increases to surpass the period of the linearized standing waves. A resonance near solution A causes the 9th Fourier mode of φ to jump discontinuously as the period increases. This resonance has little effect on the first Fourier mode.

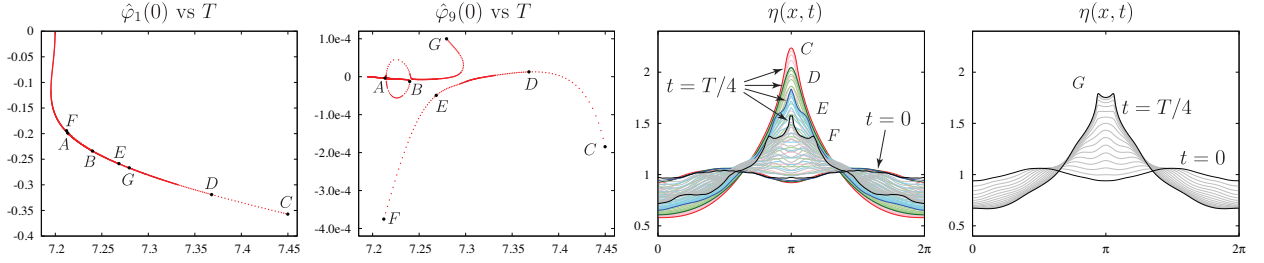


Figure 3: Several branches of standing waves were found by extrapolation across disconnections in the bifurcation curves. These disconnections are caused by resonant modes that may be interpreted physically as high-frequency standing waves superposed (nonlinearly) on the low-frequency carrier wave.

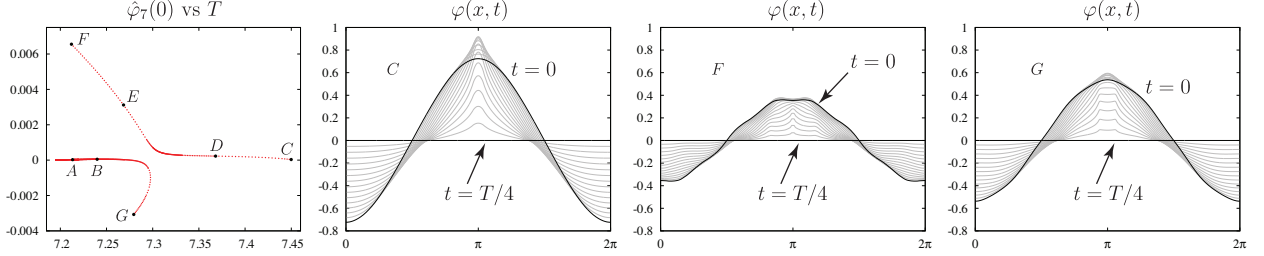


Figure 4: Bifurcation diagram showing $c_7 = \hat{\varphi}_7(0)$ versus T for standing waves of unit depth, along with snapshots of the evolution of $\varphi(x, t)$ for three of these solutions. A secondary standing wave with wave number $k = 7$ can be seen visibly superposed on $\varphi(x, 0)$ in solution F, which corresponds to the large value of c_7 at F in the diagram.

The use of Fourier modes of the initial conditions in the bifurcation diagrams is unconventional, but yields insight about the effect of resonance on the dynamics of standing waves. We observe experimentally that disconnections in the bifurcation curves correspond to higher-frequency standing waves appearing at the surface of lower-frequency carrier waves. Because the equations are nonlinear, only certain combinations of amplitude and phase can occur. We generally see two possible solutions, one in which the high and low-frequency component waves are in phase with each other, and another where they are out of phase. For example, solutions F and G in Fig. 3 can both be described as a $k = 7$ wave-number standing wave oscillating on top of a $k = 1$ carrier wave, but the smaller wave sharpens it at F and flattens it at G, being 180 degrees out of phase at F versus G when the composite wave comes to rest. (All the standing waves of this paper reach a rest state at $t = T/4$, by construction. Other types of solutions will be considered in future work [42].) In Section 4.3, we show that this disconnection between branches F and G is caused by a $(3, 7)$ harmonic resonance at fluid depth $h = 1.0397$, where the period of the $k = 1$ mode is equal to 3 times the period of the $k = 7$ mode for small-amplitude waves [4, 28].

In Fig. 4, we plot $c_7 = \hat{\varphi}_7(0)$ versus T , along with the evolution of $\varphi(x, t)$ for several solutions over time. Note that the scale on the y-axis is 20 times larger here (with c_7) than in Fig. 3 (with c_9). This is why the secondary standing waves in the plots of solutions F and G appear to have wave number $k = 7$. We also note that the disconnections at A and B are nearly invisible in the plot of c_7 vs T . This is because the dominant wave number of these branches is $k = 9$. Similarly, it is difficult to observe any of the side branches in the plot of c_1 vs T in Fig. 3 since they all sweep back and forth along nearly the same curve. We will return to this point in Section 4.3.

4.2. Nucleation of imperfect bifurcations

We next consider the effect of fluid depth on these bifurcation curves. We found the ACM method was too slow to perform this study effectively, which partly motivated us to develop the trust region shooting algorithm. As shown in Fig. 5, if the fluid depth is increased from $h = 1.0$ to $h = 1.05$, it becomes possible to track branches F and G to completion. The large amplitude oscillations in the 7th Fourier mode eventually die back down when these branches are followed past the folds at $c_7 \approx \pm 4 \times 10^{-3}$ in Fig. 5. The branches eventually meet each other at an imperfect bifurcation close to the initial bifurcation from the zero-amplitude state to the $k = 1$ standing wave solutions. This imperfect bifurcation was not present at $h = 1$. Its nucleation will be investigated in greater detail in Section 4.3. The small bifurcation loops at A and B in Fig. 3 have disappeared by the time $h = 1.05$. If we continue to increase h to

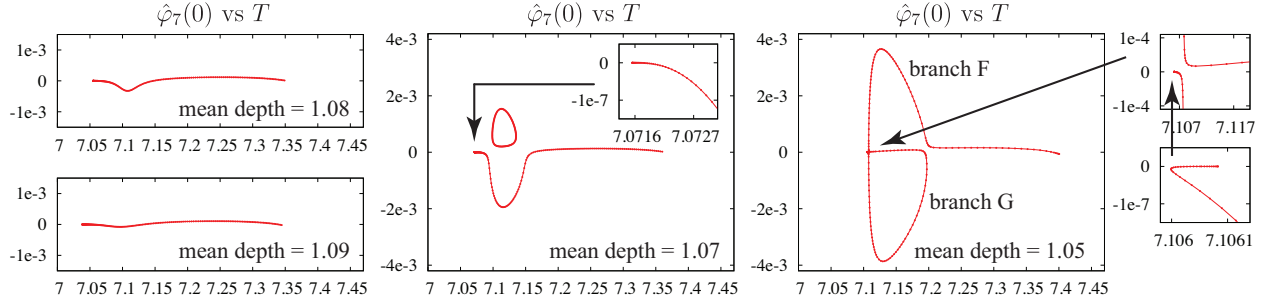


Figure 5: If the mean depth, h , is increased from 1.0 to 1.05, the loop structure between A and B in Fig. 3 disappears, and branches F and G meet each other a second time at another imperfect bifurcation. As h increases further, these loops shrink, disappearing completely by the time $h = 1.09$.

1.07, the top wing of the S-shaped bifurcation loop breaks free from the bottom wing and forms a closed loop. This loop disappears by the time h reaches 1.08. By $h = 1.09$, the $k = 7$ resonance has all but disappeared.

In Fig. 2, we saw that the period of standing waves of unit depth decreases to a local minimum before increasing with wave amplitude. Two of the plots of Fig. 5 show that this remains true for $h = 1.05$, but not for $h = 1.07$. In the latter case, the period begins increasing immediately rather than first decreasing to a minimum. This is consistent with the asymptotic analysis of Tadjbakhsh and Keller [22], which predicts that

$$\omega = \omega_0 + \frac{1}{2}\epsilon^2\omega_2 + O(\epsilon^3), \quad \omega_0^2 = \tanh h, \quad \omega_2 = \frac{1}{32}(9\omega_0^{-7} - 12\omega_0^{-3} - 3\omega_0 - 2\omega_0^5), \quad (4.36)$$

where ϵ controls the wave amplitude, and agrees with A in (4.35) to linear order. The correction term ω_2 is positive for $h < 1.0581$ and negative for $h > 1.0581$.

We will see in Section 4.3 that the nucleation of bifurcation branches between $h = 1.09$ and $h = 1.0$ is partly caused by a $(3, 7)$ harmonic resonance (defined below) at fluid depth $h = 1.0397$. As this mechanism is complicated, we also looked for simpler examples in deeper water. The simplest case we found is shown in Fig. 6. For fluid depth $h = 2$, we noticed a pair of disconnections in the bifurcation curves that were not present for $h = 2.1$. The 23rd Fourier mode of the initial condition exhibits the largest deviation from 0 on the side branches of these disconnections. However, as discussed in the next section, this is not caused by a harmonic resonance of type $(m, 23)$ for some integer m . To investigate the formation of these side branches, we swept through the region $6.64 \leq T \leq 6.68$ with slightly different values of h , using $c_0 = T$ as the bifurcation parameter. As shown in Fig. 6, when $h = 2.0455$, the bifurcation curve bulges slightly but does not break. As h is decreased to 2.045, a pair of disconnections appear and spread apart from each other. We selected $h = 2.0453$ as a good starting point to follow the side branches. As we hoped would happen, the two red side branches in the second panel of the figure met up with each other (at $c_{23} \approx 7 \times 10^{-5}$), as did the two black branches (at $c_{23} \approx -7 \times 10^{-5}$). We switched between T and c_{23} as bifurcation parameters to follow these curves. We then computed two paths (not shown) in which $c_{23} = \pm 4 \times 10^{-5}$ was held fixed as h was increased. We selected 4 of these solutions to serve as starting points to track the remaining curves in Figure 6, which have fluid depths h_2 through h_5 given in the figure. We adjusted h_2 to achieve a near three-way bifurcation. This bifurcation is quite difficult to compute as the Hessian of f becomes nearly singular; for this reason, some of the solutions had to be computed in quadruple precision to avoid falling off the curves. Finally, to find the points A and B where a single, isolated solution exists at a critical depth, we computed h as a function of (T, c_{23}) on a small 10×10 grid patch near A and B, and maximized the polynomial interpolant using Mathematica.

4.3. Degenerate and secondary bifurcations due to harmonic resonance

In this section, we explore the source of the resonance between the $k = 1$ and $k = 7$ modes in water of depth h close to 1. While harmonic resonances such as this have long been known to cause imperfect bifurcations [3, 4, 28], we are unaware that anyone has been able to track the side-branches all the way back to the origin, where they meet up with mixed-mode solutions of the type studied asymptotically by Vanden-Broeck [70] and numerically by Bryant and Stiassnie [6]. In the traveling wave case, such mixed-mode solutions are known as Wilton's ripples [71, 73]. When the fluid depth is perturbed, we find that the degenerate bifurcation splits into a primary bifurcation and two secondary bifurcations [74]. This is consistent with Bridges' work on perturbation of degenerate bifurcations in three-dimensional standing water waves in the weakly nonlinear regime [72].

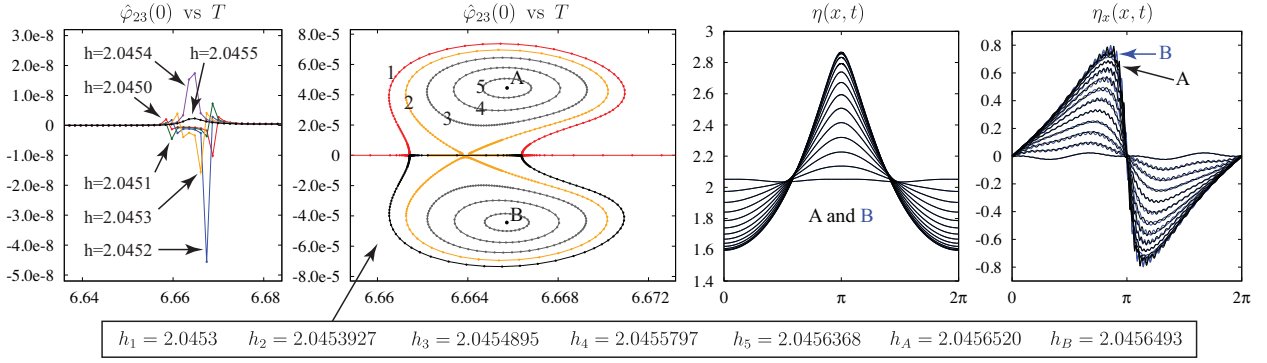


Figure 6: A pair of imperfect bifurcations were found to coalesce as fluid depth increases, leaving behind two closed loops and a smooth bifurcation curve running between them. The loops each shrink to a point and disappear as fluid depth continues to increase. Reversing the process shows that isolated solutions can nucleate new branches of solutions as fluid depth decreases. (right) The nucleated solutions A and B are nearly identical on large scales, but contain secondary, high-frequency standing waves at smaller scales that are out of phase with each other. These small oscillations become visible when the slope of the wave profile is plotted.

We begin by observing that the ratio of the periods of two small-amplitude standing waves is

$$m = \frac{T_1}{T_2} = \frac{\omega_2}{\omega_1} = \sqrt{\frac{k_2 \tanh k_2 h}{k_1 \tanh k_1 h}}. \quad (4.37)$$

If we require m to be an integer and set $k_1 = 1$, we obtain

$$k_2 \tanh k_2 h = m^2 \tanh h. \quad (4.38)$$

Following [3, 4, 28], we say there is a harmonic resonance of order (m, k_2) if h satisfies (4.38). At this depth, linearized standing waves of wave number $k = 1$ have a period exactly m times larger than standing waves of wave number $k = k_2$. This nomenclature comes from the short-crested waves literature [75, 76]; a more general framework can be imagined in which k_1 is not assumed equal to 1 and m is allowed to be rational, but we do not need such generality.

We remark that the nucleation event discussed in the previous section does not appear to be connected to a harmonic resonance. In that example, the fundamental mode must have a fairly large amplitude before the secondary wave becomes active, and the secondary wave is not a clean $k = 23$ mode. Also, no integer m causes the fluid depth of an $(m, 23)$ resonance to be close to 2.045. The situation is simply that at a certain amplitude, the $k = 1$ standing wave excites a higher-frequency, smaller amplitude standing wave that oscillates at its surface. It is not possible to decrease both of their amplitudes to zero without destroying the resonant interaction in this case.

We now restrict attention to the $(3, 7)$ harmonic resonance. Setting $m = 3$ and $k_2 = 7$ in (4.38) yields

$$7 \tanh 7h = 9 \tanh h, \quad h > 0 \quad \Rightarrow \quad h = h_{\text{crit}} \approx 1.0397189. \quad (4.39)$$

In the nonlinear problem, when the fluid depth has this critical value, we find that the $k = 7$ and $k = 1$ branches persist as if the other were not present. Indeed, the former can be computed as a family of $k = 1$ solutions on a fluid of depth $7h$. The latter can be computed by taking a pure $k = 1$ solution of the linearized problem as a starting guess and solving for the other Fourier modes of the initial conditions, as before. When this is done, after setting $\epsilon = \hat{\varphi}_1(0)$, we find that $\hat{\varphi}_3(0) = O(\epsilon^3)$, $\hat{\varphi}_5(0) = O(\epsilon^5)$, $\hat{\varphi}_7(0) = O(\epsilon^5)$, and $\hat{\varphi}_9(0) = O(\epsilon^7)$. To obtain these numbers, we used 10 values of ϵ between 10^{-4} and 10^{-3} and computed the slope of a log-log plot. The calculations were done in quadruple precision with a 32 digit estimate of h_{crit} to avoid corruption by roundoff error. If we repeat this procedure with $h = 1.0$, we find instead that $\hat{\varphi}_7(0) = O(\epsilon^7)$, $\hat{\varphi}_9(0) = O(\epsilon^9)$. Thus, the degeneracy of the bifurcation at h_{crit} appears to slow the decay rate of the 7th and higher modes, but not enough to affect the behavior at linear order.

We were surprised to discover that two additional branches also bifurcate from the stationary solution when $h = h_{\text{crit}}$. For these branches, we find that $\hat{\varphi}_k(0) = O(\epsilon^p)$, where the first several values of p are

k	p	k	p	k	p	k	p	k	p
1	1	7	1	13	3	19	5	25	7
3	3	9	3	15	3	21	3	27	5
5	3	11	5	17	5	23	5	29	5

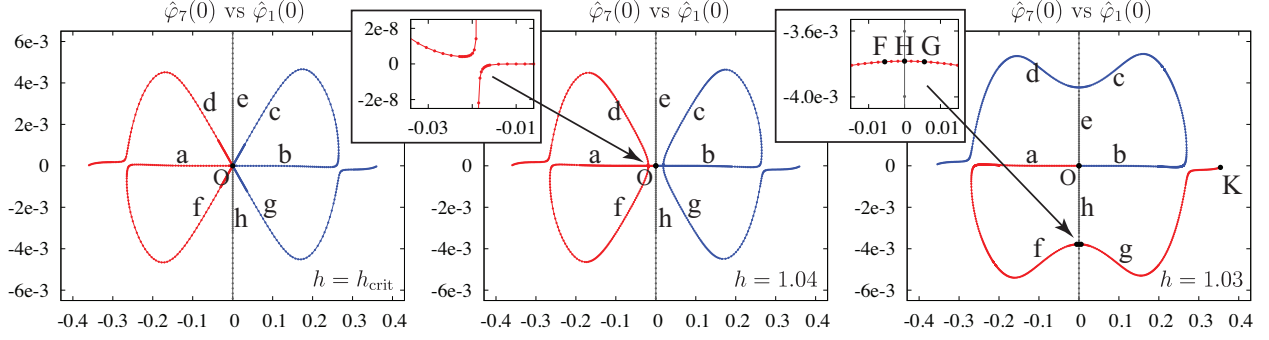


Figure 7: Perturbation of this degenerate bifurcation causes a pair of imperfect ($h > h_{\text{crit}}$) or perfect ($h < h_{\text{crit}}$) secondary bifurcations to form. Red markers are the solutions actually computed, while blue markers correspond to the same solutions, phase-shifted in space by π .

These numbers were computed as described above, with ϵ ranging between 10^{-4} and 10^{-3} . To get a clean integer for $\hat{\varphi}_{21}(0)$, $\hat{\varphi}_{27}(0)$ and $\hat{\varphi}_{29}(0)$, we had to drop down to the range $10^{-5} \leq \epsilon \leq 10^{-4}$. Using the Aitken-Neville algorithm [77] to extrapolate $\hat{\varphi}_k(0)/\epsilon^p$ to $\epsilon = 0$, we obtain the leading coefficients for the two branches:

k	$\hat{\varphi}_k(0)$	k	$\hat{\varphi}_k(0)$
1	ϵ	1	ϵ
7	$0.034152137008\epsilon + O(\epsilon^3)$	7	$-0.034152137008\epsilon + O(\epsilon^3)$
3	$-0.376330285335\epsilon^3 + O(\epsilon^5)$	3	$-0.376330285335\epsilon^3 + O(\epsilon^5)$
5	$0.065341882841\epsilon^3 + O(\epsilon^5)$	5	$-0.065341882841\epsilon^3 + O(\epsilon^5)$
9	$-0.172818320378\epsilon^3 + O(\epsilon^5)$	9	$0.172818320378\epsilon^3 + O(\epsilon^5)$
13	$0.019277463225\epsilon^3 + O(\epsilon^5)$	13	$0.019277463225\epsilon^3 + O(\epsilon^5)$
15	$-0.011062972892\epsilon^3 + O(\epsilon^5)$	15	$-0.011062972892\epsilon^3 + O(\epsilon^5)$
21	$-1.303045 \times 10^{-8}\epsilon^3 + O(\epsilon^5)$	21	$1.303045 \times 10^{-8}\epsilon^3 + O(\epsilon^5)$

(4.40)

In summary, there are four families of solutions of the nonlinear problem that bifurcate from the stationary solution. In the small amplitude limit, they approach a pure $k = 1$ mode, a pure $k = 7$ mode, and two mixed modes involving both $k = 1$ and $k = 7$ wave numbers. For convenience, we will refer to these branches as “pure” and “mixed” based on their limiting behavior in the linearized regime. The mixed mode solutions are examples of the Wilton’s ripple phenomenon [70, 71, 73] in which multiple wavelengths are present in the leading order asymptotics.

When these four branches are tracked in both directions, we end up with eight rays of solutions emanating from the equilibrium configuration, labeled a–h in Figure 7. Rays a and b consist of pure $k = 1$ mode solutions, with negative and positive amplitude, respectively, where amplitude refers to $\hat{\varphi}_1(0)$. Rays e and h are the pure $k = 7$ mode solutions, and rays c, d, f, g are the mixed mode solutions. It is remarkable that rays a and f, as well as b and c, are globally connected to each other by a large loop in the bifurcation diagram. By contrast, for the Benjamin-Ono equation [78], additional branches of solutions that emanate from a degenerate bifurcation belong to different levels of the hierarchy of time-periodic solutions than the main branches; thus, solutions on the additional branches have a different number of phase parameters, and cannot meet up with one of the main branches without another bifurcation.

We now investigate what happens to these rays when the fluid depth is perturbed. When h increases from h_{crit} to 1.04, rays e and h (the pure $k = 7$ solutions) break free from the other 6 rays. An imperfect bifurcation forms on rays a and b, linking the former to f and d, and the latter to c and g. Aside from this local reshuffling of branch connections near the stationary solution, the global bifurcation structure of $h = 1.04$ is similar to $h = h_{\text{crit}}$. In the other direction, when $h = 1.03 < h_{\text{crit}}$, rays a and b (the pure $k = 1$ solutions) disconnect from the other rays. Instead of forming imperfect bifurcations as before, rays c and d separate from the $\hat{\varphi}_7 = 0$ axis, but remain connected to ray e through a perfect bifurcation. The same is true of rays f, g and h. Thus, we have identified a case where perturbing a degenerate bifurcation causes it to break up into a primary bifurcation and two secondary bifurcations [74], either perfect ($h < h_{\text{crit}}$) or imperfect ($h > h_{\text{crit}}$).

The reason one is perfect and the other is not can be explained heuristically as follows. All the solutions on the pure $k = 7$ branch have Fourier modes $\hat{\varphi}_k(t)$, with k not divisible by 7, exactly equal to zero. These modes can be eliminated from the nonlinear system of equations by reformulating the problem as a $k = 1$ solution on a fluid of depth $7h$. This reformulation removes the resonant interaction by restricting the $k = 1$ mode (in the original formulation)

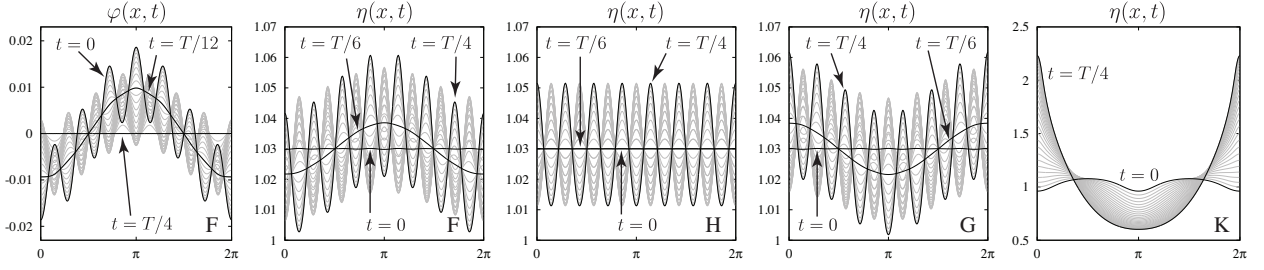


Figure 8: Solutions labeled F, G, H and K in Fig. 7 show the transition from standing waves that form crests at $x = \pi$ to those that form crests at $x = 0$ when $t = T/4$. This transition occurs where branch f meets branch g in the $h < h_{\text{crit}}$ case. For $h > h_{\text{crit}}$, branch f meets branch d at an imperfect bifurcation, and the solution at the end of path d would resemble solution K, shifted in space by π .

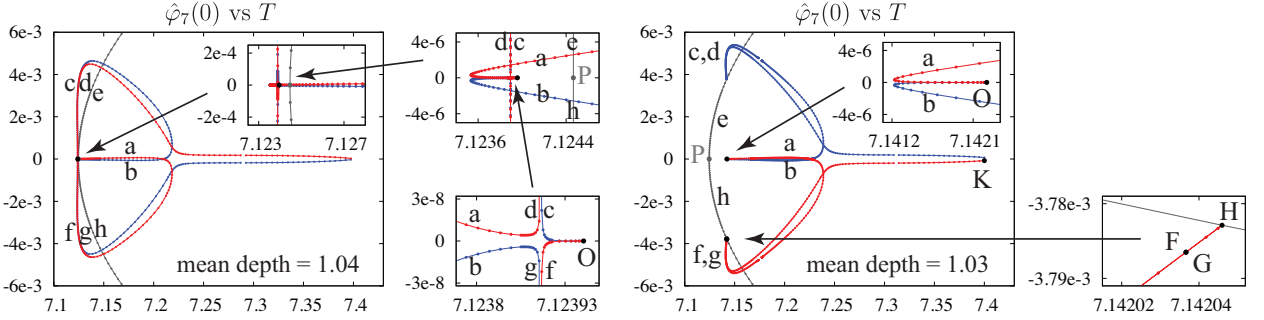


Figure 9: Solutions O and P, the bifurcation points from the equilibrium state to the pure $k = 1$ and $k = 7$ standing waves, respectively, separate from each other through a change in period as fluid depth varies from $h = h_{\text{crit}}$. The imperfect bifurcation can occur arbitrarily close to solution O by taking $h \searrow h_{\text{crit}}$. Turning points in $\hat{\varphi}_7(0)$ and T occur at solution H for $h < h_{\text{crit}}$.

to remain zero. The simplest way for this mode to become non-zero, i.e. deviate from rays e,h in Fig. 7, is through a subharmonic bifurcation (with $k = 7$ as the fundamental wavelength) in which the Jacobian J in (3.31) develops a non-trivial kernel containing a null vector $c \in \ell^2(\mathbb{N})$ with $c_1 = \hat{\varphi}_1(0) \neq 0$. Here c contains the even modes of η and the odd modes of φ at $t = 0$, as in (3.15), but with $n = \infty$. If such a kernel exists, one expects to be able to perturb the solution in this direction, positively or negatively, to obtain a pitchfork bifurcation. By contrast, solutions on the $k = 1$ branch develop non-zero higher-frequency modes through non-linear mode interactions. So while $c_1 = 0$ on the $k = 7$ branch, $c_7 \neq 0$ on the $k = 1$ branch. Since there is no way to control the influence of the 7th mode, e.g. by constraining it to be zero, there really is no “pure” $k = 1$ branch to bifurcate from, and the result is an imperfect bifurcation.

The fact that ray f is connected to g for $h < h_{\text{crit}}$, and to d for $h > h_{\text{crit}}$, has a curious effect on the form of the numerical solution at the end of the red branch, the branch of solutions actually computed, in Fig. 7. In the former case, c_1 changes sign from branch f to g, and we end up at solution K in Fig. 8, which forms a wave crest at $x = 0$ at $t = T/4$. In the latter case, c_1 remains negative from branch f to d (or branch a to d if the imperfect bifurcation is traversed without branch jumping) and we end up at a solution similar to K, but phase shifted, so that a wave crest forms at $x = \pi$ at $t = T/4$. Note that the sign of c_1 determines whether the fluid starts out flowing toward $x = \pi$ and away from $x = 0$, or vice-versa.

The transition from wave crests at $x = \pi$ to wave crests at $x = 0$ when $t = T/4$ is shown in Fig. 8. Solutions F, G and H may all be described as $k = 7$ standing waves superposed on $k = 1$ standing waves. Note that solution F bulges upward at $x = \pi$ when $t = T/4$, while solution G bulges downward there. A striking feature of these plots is that the $k = 7$ modes of φ and η nearly vanish at $t = T/12$ and $t = T/6$, respectively. This occurs because the $k = 7$ mode oscillates 3 times faster than the $k = 1$ mode. Solution H is a pure $k = 7$ solution, which means $\varphi(x, t)$ vanishes identically at $t = \frac{2m+1}{4} \left(\frac{T}{3}\right)$, $m \geq 0$, while $\hat{\eta}_7(t)$ passes through zero at $t = \frac{m}{2} \left(\frac{T}{3}\right)$, $m \geq 0$. Since solutions F and G are close to solution H, $\hat{\varphi}_7(t)$ and $\hat{\eta}_7(t)$ pass close to zero at these times, leading to smoother solutions dominated by the first Fourier mode at these times.

Figure 9 shows how the period varies along each of these solution branches. The period varies with fluid depth more rapidly for solutions on the $k = 1$ branch than on the $k = 7$ branch since the slope of $\tanh h$ is 18000 times larger than that of $\tanh 7h$ when $h \approx 1$. As a result, bifurcation point O (to the $k = 1$ branch) moves visibly when h changes from 1.03 to 1.04, while bifurcation point P (to the $k = 7$ branch) hardly moves at all. We also see that the period

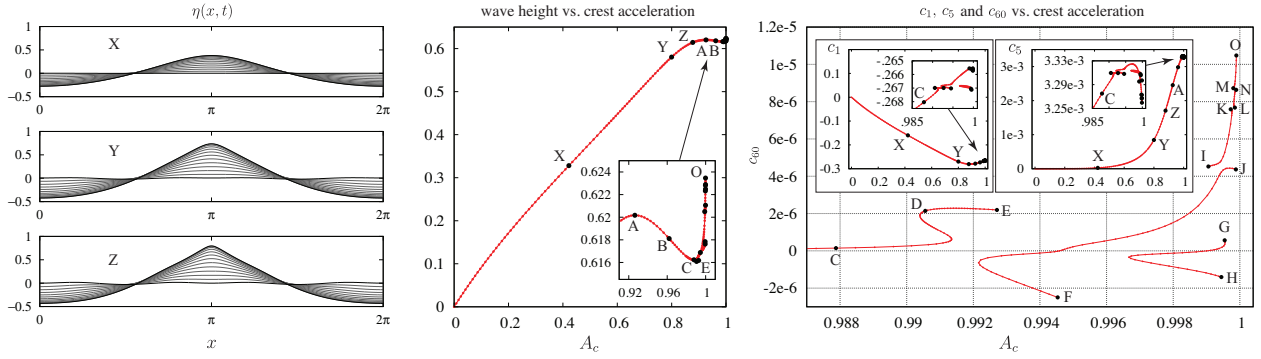


Figure 10: Snapshots of several standing waves over a quarter period in water of infinite depth, along with bifurcation diagrams showing where they fit in. (center) Conventional bifurcation diagram showing wave height versus crest acceleration. The turning point at A was discovered by Mercer and Roberts [2] while the turning point at C and subsequent bifurcation structure were discovered by Wilkening [17]. The wave height h eventually exceeds the local maximum at A. (right) The continuation parameters actually used were c_1 , c_5 , c_{60} and T rather than h or A_c .

increases with amplitude on branches e and h. By contrast, on branches a and b, it decreases to a local minimum before increasing with amplitude. This is consistent with the asymptotic analysis of Tadjbakhsh and Keller discussed previously; see (4.36) above. Finally, we note that both T and c_7 have a turning point at solution H, the bifurcation point connecting branches f and g to branch h. This causes paths f and g to lie nearly on top of each other for much of the bifurcation diagram. Other examples of distinct bifurcation curves tracing back and forth over nearly the same paths are present (but difficult to discern) in Figures 7 and 9 when $h = 1.03$, and will be discussed further in Section 5.

4.4. Breakdown of self-similarity and the Penney and Price conjecture

In Sections 4.2 and 4.3 above, we have seen that increasing the fluid depth causes disconnections in the bifurcation diagrams to “heal,” and it is natural to ask if any will persist to the infinite depth limit. The answer turns out to be yes, which is not surprising from a theoretical point of view since infinite depth standing waves are completely resonant [20], involving state transition operators with infinite dimensional kernels and a small-divisor problem on the complement of this kernel. Nevertheless, examples of such disconnections have only recently been observed in numerical simulations [17], and show no evidence of being densely distributed along bifurcation curves. In this section, we expand on the results of [17], filling in essential details and providing new material not discussed there. The scarcity of observable disconnections will be discussed further in the conclusion section.

The main question addressed in [17] is whether standing waves of extreme form approach a limiting wave profile with a geometric singularity at the wave crest when the bifurcation curve terminates. This type of question has a long history, starting with Stokes [79, 80], who predicted that the periodic traveling wave of greatest height would feature wave crests with sharp, 120° interior crest angles. While there are some surprises concerning oscillatory asymptotic behavior at the crest of the almost highest traveling wave [81, 82, 17], it has been confirmed both theoretically [83] and numerically [84, 85] that a limiting extreme traveling wave does exist, and possesses a sharp 120° wave crest. For standing waves, a similar conjecture was made by Penney and Price in 1952 [13], who predicted that the limiting extreme wave would develop sharp, 90 degree interior crest angles each time the fluid comes to rest. As discussed in the introduction, numerous experimental, theoretical and numerical studies [14, 15, 16, 8, 29, 2, 7] have reached contradictory conclusions on the limiting behavior at the crests of extreme standing waves.

Penney and Price expected wave height, defined as half the maximum crest-to-trough height, to increase monotonically from the zero-amplitude equilibrium wave to the extreme wave. Mercer and Roberts found that wave height reaches a turning point, achieving a local maximum of $h = 0.62017$ at $A_c = 0.92631$, where A_c is the downward acceleration of a fluid particle at the wave crest at the instant the fluid comes to rest (assuming $g = 1$ in (2.1)). Since h is not a monotonic function, they proposed using crest acceleration as a bifurcation parameter instead. However, as shown in Fig. 10, crest acceleration also fails to be a monotonic function. The bifurcation curve that was supposed to terminate at the extreme wave when A_c reaches 1 becomes fragmented for $0.99 < A_c < 1$. Just as in the finite depth case, this fragmentation is due to resonant interactions between the large-scale carrier wave and various smaller-scale, secondary standing waves that appear at the surface of the primary wave. Figure 11 shows several examples of the oscillatory structures that are excited by resonance, both in space and in time. The amplitude of the higher-frequency oscillations are small enough in each case that the vertical position of a particle traveling from trough to crest increases

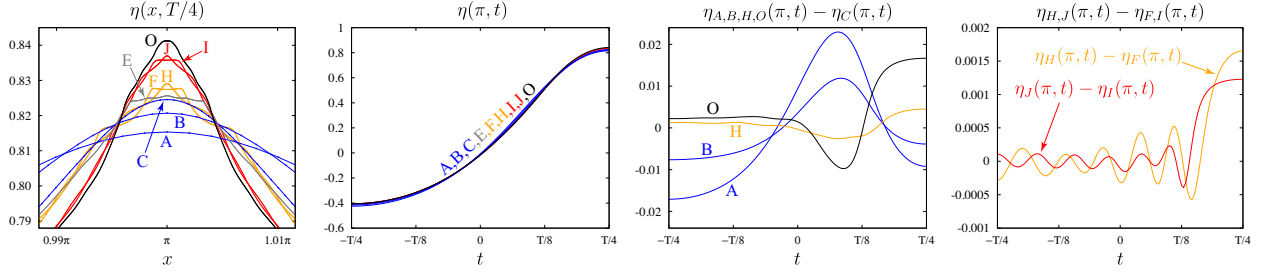


Figure 11: Oscillatory structures near the wave crest, and time-evolution of a particle from trough to crest, for several extreme standing waves. Labels correspond to the bifurcation diagrams in Figure 10. These solutions take the form of higher-frequency standing waves superimposed nonlinearly on lower-frequency carrier waves. The higher-frequency oscillations occur both in space and time.

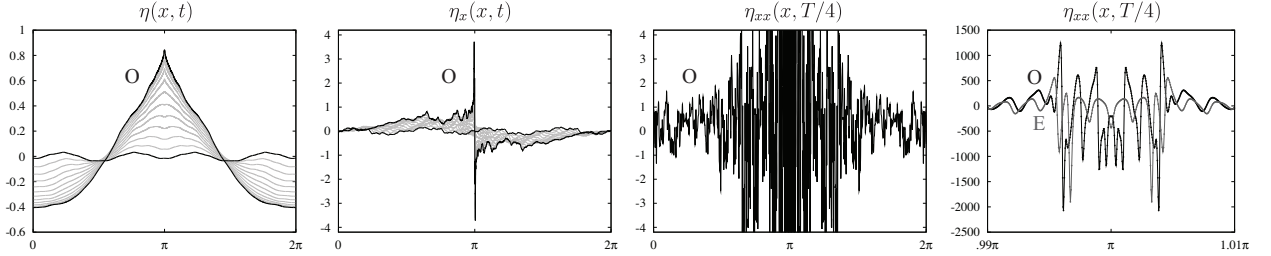


Figure 12: Evolution of surface height and its derivatives over a quarter period for solution O in Figure 10. The plots at right of η_{xx} are shown only at time $T/4$ for clarity. In the far right panel, we also plotted solution E for comparison. Each solution that terminates a branch in the bifurcation diagram is highly oscillatory; we followed the branches to the point that the computations became too expensive to continue further.

monotonically in time; however, plotting differences of solutions on nearby branches as a function of time reveals the temporal behavior of the secondary standing waves. We note that the frequency of oscillation of the secondary waves (near $x = \pi$) decreases as t approaches $T/4$. This seems reasonable as fluid particles at the crest are nearly in free-fall at this time when A_c is close to 1; thus, the driving force of the secondary oscillations is low there. In shallow water, the secondary oscillations are often strong enough to lead to non-monotonic particle trajectories from trough to crest (see Section 4.5).

If a limiting wave profile does not materialize as A_c approaches 1, a natural question arises as to what will terminate the bifurcation curves. In [17], it was emphasized that oscillations at the crest tip prevent self-similar sharpening to a corner, as happens in the traveling case. We note here that the entire wave profile, not just the crest tip, develops high-frequency oscillations on small scales toward the end of each bifurcation curve. This is illustrated in Fig. 12, and suggests that if these bifurcation curves do end somewhere, without looping back to merge with another disconnection, it may be due to solutions becoming increasingly rough, with some Sobolev norm diverging in the limit. We also remark that since many of these standing waves come close to forming a 90° corner, there may well exist nearly time-periodic solutions that do pass through a singular state. Taylor's thought experiment [14] in which water is piled up in a crested configuration and released from rest could be applied to a sharply crested perturbation of the rest state of one of our standing waves. However, like Taylor, we see no reason that 90° would be the only allowable crest angle. It is conceivable that 90° is the only angle for which smooth solutions can propagate forward from a singular initial condition, but we know of no such results.

The increase in roughness of the solutions as crest acceleration approaches 1 may also be observed by plotting Fourier mode amplitudes for various solutions along the bifurcation curve. In Fig. 13, we compare the Fourier spectrum of η at $t = 0$ and $t = T/4$ for solutions O and A. In both of these simulations, we parametrized the curve non-uniformly, as in (2.10), to increase resolution near the crest tip. Thus, a distinction must be made between computing Fourier modes with respect to x versus α :

$$\hat{\eta}_k(t) = \frac{1}{2\pi} \int_0^{2\pi} \eta(x, t) e^{-ikx} dx, \quad \text{or} \quad \hat{\eta}_k(t) = \frac{1}{2\pi} \int_0^{2\pi} \eta(\xi_{l(t)}(\alpha), t) e^{-ik\alpha} d\alpha. \quad (4.41)$$

In this figure, we use the latter convention, since $\eta \circ \xi_l$ and $\varphi \circ \xi_l$ are the quantities actually evolved in time, and the decay rate of Fourier modes is faster with respect to α . At $t = 0$, the two formulas in (4.41) agree since we require

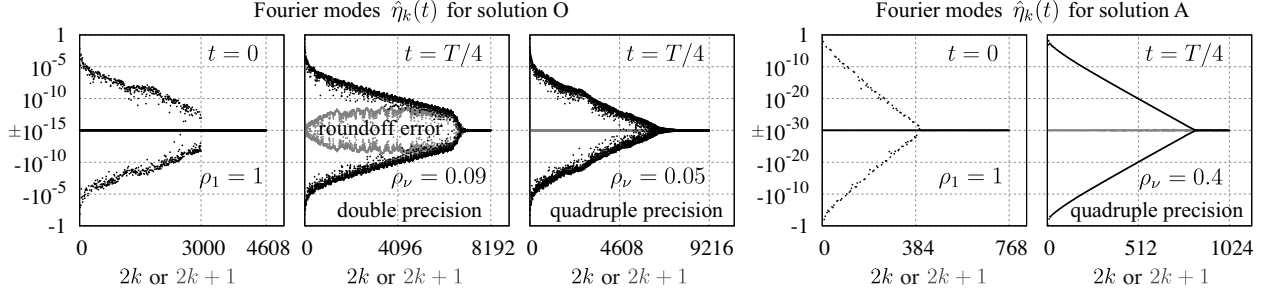


Figure 13: The Fourier modes of η (shown) and φ (not shown) are monitored to decide how many grid points are needed to resolve the solution. The parameter ρ_1 controls the nonuniform spacing of gridpoints via (2.10). The real (black) and imaginary (grey) parts of $\hat{\eta}_k(t)$ are plotted in positions $2k$ and $2k + 1$, respectively. (Left) the minimization was performed in double precision to obtain these initial conditions. The result was checked in quadruple precision to eliminate roundoff error. (Right) the minimization was performed in quadruple precision, yielding $f = 2.1 \times 10^{-60}$.

$\xi_1(\alpha) = \alpha$. For solution O, the Fourier modes of the initial conditions decay to $|c_k| < 10^{-12}$ for $2k \geq 3000$. At $t = T/4$ we have $\max(|\hat{\eta}_k|, |\hat{\varphi}_k|) < 10^{-12}$ for $2k \geq 6500$ with $\rho_\nu = 0.09$. For solution A, we have $|c_k| < 10^{-29}$ for $2k \geq 400$ and $\max(|\hat{\eta}_k|, |\hat{\varphi}_k|) < 10^{-29}$ for $2k \geq 800$ at $t = T/4$ with $\rho_\nu = 0.4$. Here $T = 1.629324$ for solution O and $T = 1.634989$ for solution A. The mesh parameters used in these simulations are listed in Table 1. We remark that for solutions such as O with fairly sharp wave crests, decreasing ρ_ν generally leads to faster decay of Fourier modes, but also amplifies roundoff errors due to closer grid spacing near the crest. Further decrease of ρ_ν in the double-precision calculation does more harm than good.

solution	ν	θ_1	θ_2	θ_3	θ_4	ρ_1	ρ_2	ρ_3	ρ_4	n	M_1	M_2	M_3	M_4	N_1	N_2	N_3	N_4
A (quad)	2	0.2	0.8	-	-	1.0	0.4	-	-	200	768	1024	-	-	24	144	-	-
O (double)	4	0.2	0.3	0.3	0.2	1.0	0.4	0.1	0.09	1500	4608	6144	6912	8192	192	432	576	480
O (quad)	4	0.1	0.3	0.4	0.2	1.0	0.25	0.08	0.05	1500	6144	7500	8192	9216	60	216	384	240

Table 1: Mesh parameters used to compute solutions A and O in Figures 13 and 14.

The effect of roundoff-error and the 36th order filter can both be seen in the second panel of Fig. 13. In exact arithmetic, $\eta(x, t)$ and $\varphi(x, t)$ would remain even functions for all time. However, in numerical simulations, the imaginary parts of $\hat{\eta}_k(t)$ and $\hat{\varphi}_k(t)$ drift away from zero, giving a useful indicator of how much the solution has been corrupted by roundoff error. The filter (2.14) has little effect on the first 70 percent of the Fourier modes, but strongly damps out the last 15 percent. By monitoring the decay of Fourier modes through plots like this, one can ensure that the simulations are fully resolved, and that filtering does not introduce more error than is already introduced by roundoff error. We also monitor energy conservation,

$$E(t) = \frac{1}{2} \int_0^{2\pi} [\varphi(x, t) \mathcal{G}\varphi(x, t) + g\eta(x, t)^2] dx,$$

choosing time-steps small enough that E remains constant to as many digits as possible, typically 14 in double-precision and 29 in quadruple precision. Note that \mathcal{G} depends on time through η .

Because solution A remains smoother and involves many fewer Fourier modes than solution O, it was possible for us to perform the entire computation in quadruple precision arithmetic. This allowed us to reduce f in (3.17) to 2.1×10^{-60} . As shown in Fig. 14, the velocity potential of this solution drops from $O(1)$ at $t = 0$ to less than 3×10^{-29} at $t = T/4$, in the uniform norm. While it was not possible to perform the minimization for solution O in quadruple precision arithmetic (due to memory limitations of the GPU device), we were able to check the double-precision result in quadruple precision to confirm that f is not under-predicted by the minimization procedure. Because the DOPRI8 and SDC15 methods involve 12 and 99 internal Runge-Kutta stages per time-step, respectively, more function evaluations were involved in advancing the quadruple-precision calculations through time even though N_I is larger in the double-precision calculations. As shown in Fig. 14, the oscillations in $\varphi(x, T/4)$ remain fully resolved in the quadruple precision calculation; thus, $f = 8.6 \times 10^{-27}$ is an accurate measure of the squared error. The predicted

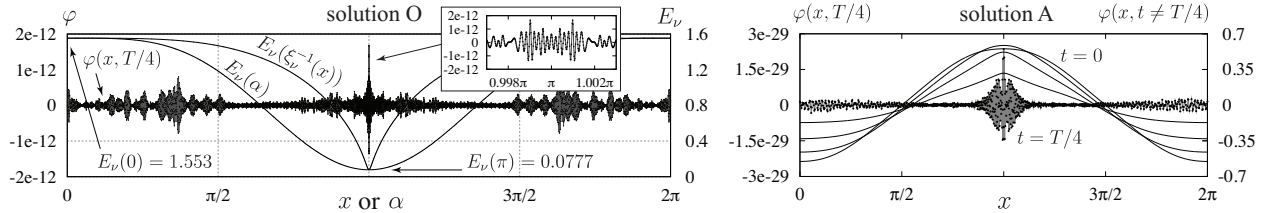


Figure 14: Plots of the residual $\varphi(x, T/4)$ for solutions O and A. (left) When minimized in double-precision arithmetic, we obtain $f = 1.3 \times 10^{-26}$. Shown here is a re-computation of the solution in quadruple precision on a finer mesh using the same initial conditions. This yields $f = 8.6 \times 10^{-27}$, which is even smaller than predicted in double-precision. Re-spacing the grid maps the curve $E_v(\alpha)$ to $E_v(\xi_v^{-1}(x))$, improving the resolution that can be achieved with 9216 gridpoints. Note that the oscillations in $\varphi(x, T/4)$ are fully resolved. (right) The minimization was performed in quadruple-precision arithmetic, yielding $f = 2.1 \times 10^{-60}$. The velocity potential is nearly 30 orders of magnitude smaller at $t = T/4$ than at $t = 0$.

value of f in double-precision (obtained by minimizing f) was $f = 1.3 \times 10^{-26}$. Since minimizing f entails eliminating as many significant digits of $\varphi(x, T/4)$ as possible, the resulting value of f is not expected to be highly accurate. What is important is that minimizing f in double-precision does not grossly underestimate its minimum value. In fact, its value is often over-estimated, as occurred here. This robustness is a major benefit of posing the problem as an *overdetermined* non-linear system. The only way to achieve a small value of f is to accurately track a solution of the PDE for which the exact f is small. Roundoff errors and truncation errors will cause the components of r in (3.17) to drift away from zero, leading to an incompatible system of equations with minimum residual of the order of the accumulated errors.

There is a big advantage to choosing $t = 0$ to occur at the midpoint between rest states rather than at a rest state. The reason is that many more Fourier modes are needed to represent η when the wave crest is relatively sharp, which for us occurs when t is near $T/4$. For example, solutions O and A in Fig. 13 have more than twice as many active Fourier modes at $t = T/4$ as they did at $t = 0$, even using a non-uniform grid to better resolve the crested region. Setting up the problem this way leads to fewer Fourier modes of the initial condition to solve for, and increases the number of non-linear equations. Thus, the system is more overdetermined, adding robustness to the computation.

We conclude this section by mentioning that “branch jumping” is very easy to accomplish (and hard to avoid) in the numerical continuation algorithm. For strong disconnections such as at solution B in Fig. 2, it is sometimes necessary to backtrack away from the disconnection and then take a big step, hoping to land beyond the gap. Since we measure the residual error in an overdetermined fashion, it is obvious if we land in a gap where there is no time-periodic solution — the minimum value of f remains large in that case. However, most disconnections can be traversed without backtracking, or even knowing in advance of their presence. The disconnections in Figure 10 were all discovered by accident in this way. Once a disconnection is observed, we can go back and follow side branches to look for global re-connections or new families of time-periodic solutions.

4.5. Counter-propagating solitary waves in shallow water

In previous sections, we saw that decreasing the fluid depth causes nucleation of loop structures in the bifurcation curves that nearly (or actually) meet at imperfect (or perfect) bifurcations. Some of these disconnections persist in the infinite depth limit. We now consider the other extreme of standing waves in very shallow water.

In Figure 15, we track the $k = 1$ family of standing waves out of the linear regime for water of depth $h = 0.05$ and spatial period 2π . The period of the solutions in the linear regime is $T = 2\pi / \sqrt{\tanh 0.05} = 28.1110$, compared to $T = 7.19976$ when $h = 1$ and $T = 2\pi = 6.28319$ when $h = \infty$. Thus, the waves travel much slower in shallow water. We also see that T decreases with amplitude as the waves leave the linear regime, consistent with Tadjbakhsh and Keller’s result, Equation (4.36) above, that the sign of the quadratic correction term in angular frequency is positive for $h < 1.0581$. Many more disconnections have appeared in the bifurcation diagrams at this depth than were observed in the cases $h \approx 1.0$ and $h = \infty$ considered above. It was not possible to track all the side branches that have emerged to see if they reconnect with each other. However, each time we detected that the minimization algorithm had jumped from one branch to another, we did backtrack to fill in enough points to observe which modes were excited by the resonance. In general, higher-frequency Fourier modes of the initial condition possess more disconnections, even though all the bifurcation curves describe the same family of solutions. For example, in Fig. 15, we see that $\hat{\varphi}_{17}(0)$ has much stronger disconnections than $\hat{\varphi}_1(0)$, and those of $\hat{\eta}_{36}(0)$ are stronger still. This suggests that high-frequency resonances have little effect on the dynamics of lower-frequency modes. Nevertheless, there is *some* effect, since even

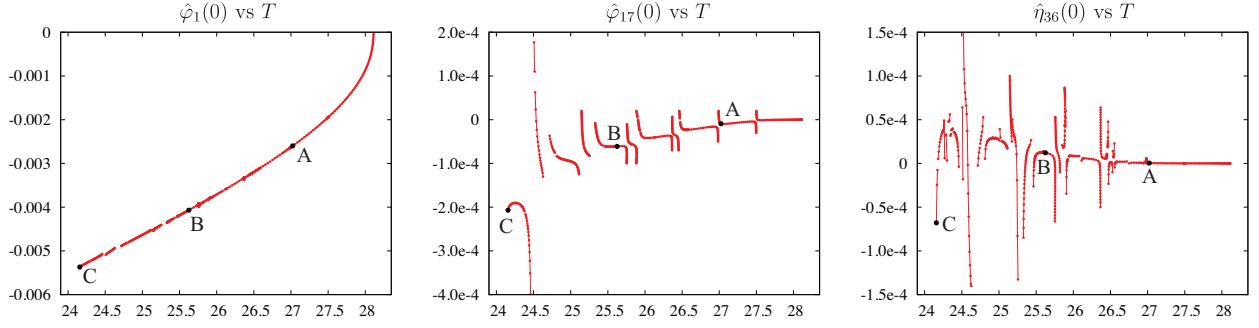


Figure 15: Bifurcation diagrams showing the dependence of $\hat{\varphi}_1(0)$, $\hat{\varphi}_{17}(0)$, and $\hat{\eta}_{36}(0)$ on T for a family of standing water waves in shallow ($h = 0.05$) water. Many more disconnections are visible at this depth than were observed in the $h = 1.0$ and $h = \infty$ cases above.

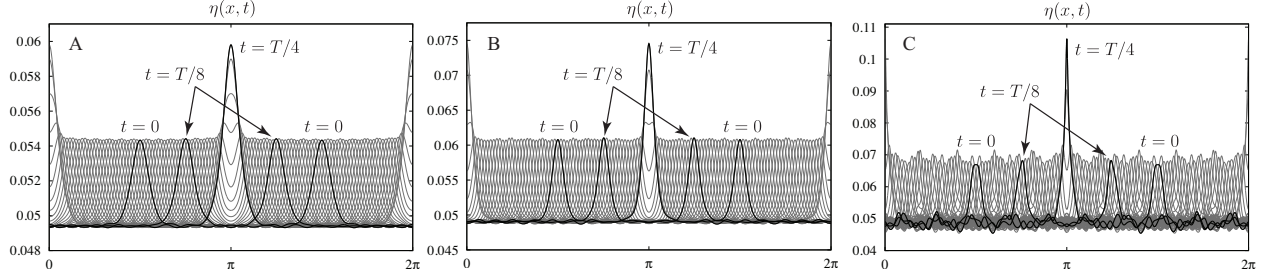


Figure 16: Standing waves in shallow water take the form of counter-propagating solitary waves that interact elastically. The low-amplitude radiation normally associated with inelastic collisions is already present before the interaction, and does not increase as a result of the interaction. In solutions A and B, this radiation consists of small-amplitude, high-frequency standing waves over which the solitary waves travel. In solution C, this radiation is a chaotic mix of standing and counter-propagating traveling waves of different wave numbers.

$\hat{\varphi}_1(0)$ exhibits visible disconnections, and in fact has some gaps in T where solutions could not be found. We interpret these gaps as numerical manifestations of the Cantor-like structures that arise in analytical studies of standing water waves due to small divisors [24, 20]. This will be discussed further in the conclusion section.

In Figure 16, we show time-elapsing snapshots of the standing wave solutions labeled A–C in Figure 15. These standing waves no longer lead to large scale sloshing modes in which the fluid rushes from center to sides and back in bulk. Instead, a pair of counter-propagating solitary waves travel back and forth across the domain, alternately colliding at $x = \pi$ and $x = 0$ at times $t = T/4 + (T/2)\mathbb{Z}$. In the unit depth case above, we observed in Figure 3 that disconnections in the bifurcation curve correspond to secondary standing waves appearing with one of two phases at the surface of a primary carrier wave. The same is true of these solitary wave interactions. While it is difficult to observe in a static image, movies of solutions A and B in Figure 16 reveal that the primary solitary waves travel over smaller standing waves with higher wave number and angular frequency. As a result, a fluid particle at $x = \pi$ will oscillate up and down with the secondary standing wave until the solitary waves collide, pushing the particle upward a great distance. By contrast, in the infinite-depth case, we saw in Figure 11 that $\eta(\pi, t)$ increases monotonically from trough to crest in spite of the secondary waves. Each time a disconnection in Figure 15 is crossed, the background standing wave (or some of its component waves) change phase by 180° . Solution B is positioned near the center of a bifurcation branch, far from major disconnections in the bifurcation curves. As a result, the water surface over which the solitary waves travel remains particularly calm for solution B. By contrast the background waves of solution C are quite large in amplitude, with many active wave numbers. A Floquet stability analysis, presented elsewhere [42], shows that solutions A and B are linearly stable to harmonic perturbations while solution C is unstable.

4.6. Gravity-capillary standing waves

In this section, we consider the effect of surface tension on the dynamics of standing water waves. We restrict attention to waves of the type considered by Concus [23] and Vanden-Broeck [70], leaving collisions of gravity-capillary waves [53] for future work [42]. The only change in the linearized equations (4.34) when surface tension is

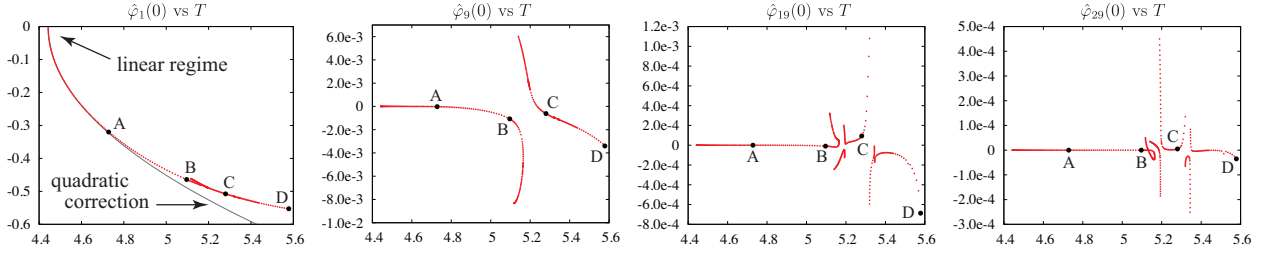


Figure 17: Bifurcation diagrams showing the dependence of various Fourier modes of the initial conditions on the period for standing water waves with surface tension. The bifurcation curve splits into several disjoint branches between solutions B and C as resonant waves appear on the fluid surface. The curve labeled ‘quadratic correction’ is given in Equation (4.43).

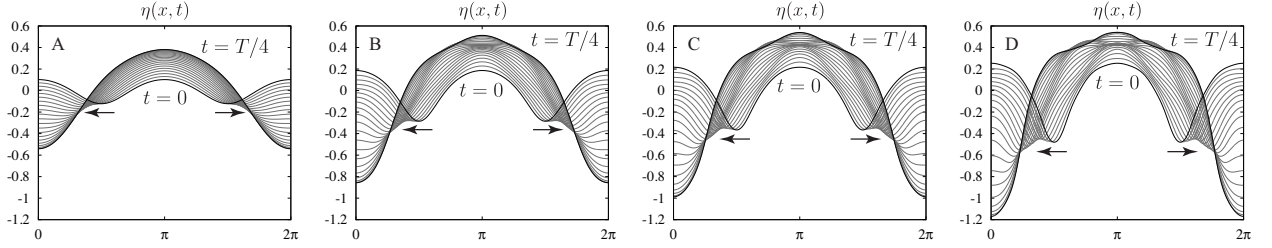


Figure 18: Time-elapsed snapshots of four standing waves over a quarter-period. At $t = 0$, a pair of counter-propagating depression waves move away from each other as the fluid flows to the center. Solutions B, C and D exhibit higher-frequency standing waves oscillating on the surface of the low-frequency carrier wave. All of the solutions reach a rest state where $\varphi \equiv 0$ at $t = T/4$.

included is that $\dot{\varphi}_t = P[-g\dot{\eta} + (\sigma/\rho)\dot{\eta}_{xx}]$. The standing wave solutions of the linearized problem continue to have the form (4.35), but with

$$\omega^2 = \left(g + \frac{\sigma}{\rho}k^2\right)k \tanh kh, \quad A/B = \sqrt{k \tanh kh / [g + (\sigma/\rho)k^2]}. \quad (4.42)$$

We choose length and time-scales so that $g = 1$ and $\sigma/\rho = 1$. For simplicity, we consider only the $k = 1$ bifurcation in the infinite depth case, and continue to assume all functions are 2π -periodic in space. In this configuration, the period of the linearized standing waves is $T = 2\pi/\sqrt{2} \approx 4.443$. For real water (assuming $\sigma = 72$ dyne/cm), 4.443 units of dimensionless time corresponds to 0.0739 seconds, and 2π spatial units corresponds to 1.7 cm.

The results are summarized in Figure 17. As the bifurcation parameter, $c_1 = \hat{\varphi}_1(0)$, increases in magnitude beyond the realm of linear theory, the period increases, just as in the zero surface tension case for $h = \infty$. Quantitatively, our results agree with Concus’ prediction [23] that

$$T = \sqrt{2}\pi \left(1 + \frac{197}{320}c_1^2\right), \quad c_1 = \hat{\varphi}_1(0) \quad (4.43)$$

in the infinite depth case when the surface tension parameter $\delta := \sigma k^2 / (\sigma k^2 + \rho g)$ is equal to $1/2$. Equation (4.43) is plotted in the left panel of Figure 17 for comparison. Shortly after solution B ($c_1 = -0.464$, $T = 5.10$), a complicated sequence of imperfect bifurcations occurs in which several disjoint families of solutions pass near each other. Comparison of solutions B, C and D in Figure 18 suggests that these disconnections are due to the excitation of different patterns of smaller-scale capillary waves oscillating on the free surface. An interesting difference between these standing waves and their zero surface-tension counterparts (e.g. in Figure 2) is that the ‘solitary’ waves that appear in the transition periods between rest states of maximum amplitude are inverted. Thus, we can think of these solutions as counter-propagating depression waves [86, 87] that are tuned to be time-periodic, just as the zero surface-tension case leads to counter-propagating Stokes waves. The depression waves travel outward as fluid flows to the center, whereas the Stokes waves travel inward, carrying the fluid with them. Figure 19 shows snapshots of particle trajectories for solution C, color coded by pressure. The methodology for computing this pressure is given at the end of Appendix A. Negative pressure (relative to the ambient air pressure p_0 in (2.4), which is set to zero for convenience) arises beneath the depression waves as they pass, which leads to larger pressure gradients, faster wave speeds, and shorter periods than were seen in previous sections.

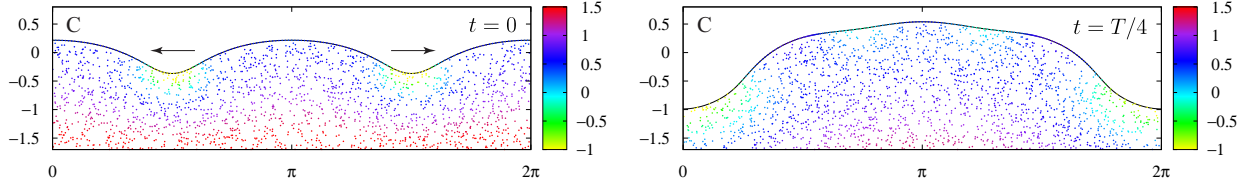


Figure 19: A more detailed view of solution C from Figure 18 at times $t = 0$ and $t = T/4$ showing regions of negative pressure beneath depression waves. These images are taken from movies in which passively advected particles have been added to the fluid for visualization, color coded by pressure using (A.12). A secondary standing wave leads to visible variations in curvature and pressure at time $T/4$.

4.7. Performance comparison

We conclude our results with a comparison of running times for the various algorithms and machines used to generate the data reported above. Our machines consist of a laptop, a desktop, a server, a GPU device, and a supercluster. The laptop is a Macbook Pro, 2.53 GHz Intel Core i5 machine. The desktop is a Mac Pro with two quad-core 2.8 GHz Intel Nehalem processors. The rackmount server has two six-core 3.33 GHz Intel Westmere processors and an NVidia M2050 GPU, and is running Ubuntu Linux. The cluster is the Lawrencium cluster (LR1) at Lawrence Berkeley National Laboratory. Each node of the cluster contains two quad-core 2.66 GHz Intel Harpertown processors. Intel’s math kernel library and scalapack library were used for the linear algebra on Lawrencium.

Our first test consists of computing the first 120 deep-water standing wave solutions reported in Figure 10 (up through solution B). The running times increase with amplitude due to an increase in the number of gridpoints (M), timesteps (N), and unknown Fourier modes of the initial conditions (n). The parameters used in this test are given in Table 2, with running times reported in the left panel of Figure 20. For each index range, we computed the average time required to reduce f below 10^{-25} (or 10^{-50} in quadruple precision), using linear extrapolation from the previous two solutions as a starting guess. In the Adjoint Continuation Method, the first solution in each range (with index 101, 150, 174, etc.) takes much longer than subsequent minimizations. This is because we re-build the inverse Hessian from scratch when the problem size changes, but not from one solution to the next in a given index range. This is illustrated in the figure by plotting the maximum and median number of seconds required to find a solution in a given index range, along with the average.

For these smaller problems, the DOPRI5 and DOPRI8 schemes are of comparable efficiency for double-precision accuracy. We used the former for this particular test. In quadruple precision, we switched to the SDC15 scheme, which is more efficient than DOPRI5 and DOPRI8 in reducing f below 10^{-50} . We also doubled M and n in the quadruple-precision runs. The MINPACK benchmark results were optimized as much as possible (using the GPU with Error Correcting Code (ECC) turned off) to give as fair a comparison as possible. For the benchmark, the Jacobian was computed via forward differences, as in (3.33). The ACM method works well on small problems, but starts to slow down relative to the benchmark around $M = 1024$. The trust region shooting method is much faster than the ACM (and the benchmark) due to the fact that all the columns of the Jacobian employ the same Dirichlet to Neumann operator at each timestep. Thus, we save a factor of n in setup costs by computing n columns of the Jacobian simultaneously. Moreover, most of the work can be organized to run at level 3 BLAS speed. Note that the GPU is slower than the

index range	n	M	N	N_{quad}	bif par	start	end	T_{start}	T_{end}
101–150	20	128	60	24	$\hat{\varphi}_1(0)$	−0.004	−0.2	1.5708	1.6034
150–174	32	192	96	36	$\hat{\varphi}_1(0)$	−0.2	−0.26	1.6034	1.6265
174–184	50	256	96	48	$\hat{\varphi}_1(0)$	−0.26	−0.275	1.6265	1.6332
184–194	54	384	120	60	$\hat{\varphi}_5(0)$	0.001071	0.001856	1.6332	1.6359
194–200	64	512	144	72	$\hat{\varphi}_5(0)$	0.001856	0.002117	1.6359	1.6358
200–210	75	768	180	96	$\hat{\varphi}_5(0)$	0.002117	0.002515	1.6358	1.6348
210–220	96	1024	240	120	$\hat{\varphi}_5(0)$	0.002515	0.002981	1.6348	1.6326

Table 2: Parameters used in the performance comparison for small problems. Here “start” and “end” give the values of the bifurcation parameter (bif par) at the endpoints of the corresponding segment of the bifurcation curve. The solutions at these endpoints (with index 150, 174, 184, etc.) are computed twice, once on the coarse mesh and once on the fine mesh. T_{start} and T_{end} are the periods at the endpoints. N_{quad} is the number of timesteps (of the SDC scheme) used in the quadruple precision calculations. M_{quad} and n_{quad} were set equal to $2M$ and $2n$, respectively.

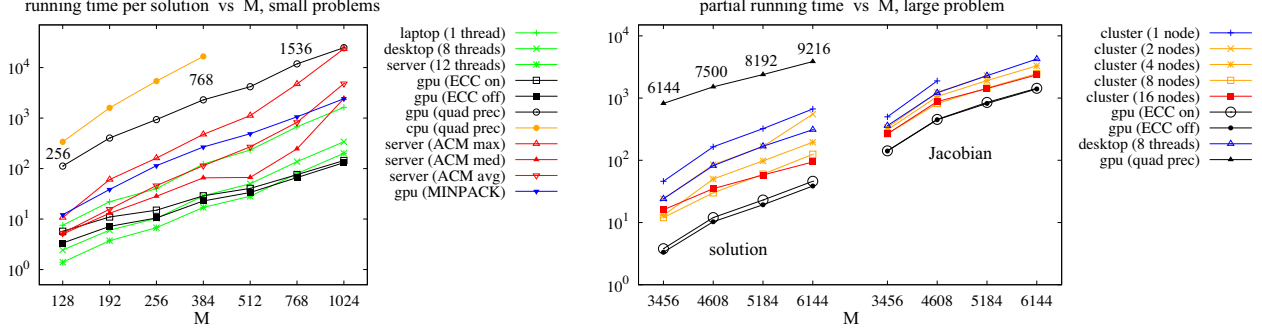


Figure 20: Performance of the algorithms on various architectures. (left) Each data point is the average running time (in seconds per solution) for solutions in each index range listed in Table 2. For the Adjoint Continuation Method (ACM), which takes much longer for the first solution than subsequent solutions due to re-use of the Hessian information, we also report the longest running time and the median running time. (right) Time taken in each segment of the mesh-refinement strategy to evolve solution O in Figure 12 through 1/60th of a quarter-period. The parameters for each segment are given in Table 3. The times listed for the Jacobian are the cost of evolving all 1200 columns through time $T/240$.

	ν	θ_1	θ_2	θ_3	θ_4	ρ_1	ρ_2	ρ_3	ρ_4	n	M_1	M_2	M_3	M_4	d_1	d_2	d_3	d_4	scheme
double	4	0.2	0.2	0.2	0.4	1.0	0.4	0.12	0.09	1200	3456	4608	5184	6144	10	20	30	40	DOPRI8
quad	4	0.1	0.3	0.4	0.2	1.0	0.25	0.08	0.05	1500	6144	7500	8192	9216	10	12	16	20	SDC15

Table 3: Parameters used in the performance comparison for a large problem (solution O of Figure 12). Here d_l is the number of timesteps to advance the solution through one sixtieth of a quarter period ($T/240$). The total number of timesteps on segment l is $N_l = 60\theta_l d_l$ in this case, while the number of function evaluations is $12N_l$ for DOPRI8 and $99N_l$ for SDC15.

multi-core CPU in double-precision for small problems, but eventually wins out as the opportunity for parallelism increases. In quadruple-precision, the GPU is substantially faster than the CPU for all problem sizes tested as there is more arithmetic to be done relative to communication costs.

Our second test consists of timing each phase of the computation of solution O in Figure 12. The parameters used for the performance comparison are given in Table 3. For the double-precision calculation, we later refined the mesh to the values listed in Table 1 in Section 4.4; however, this was done on one machine only. (The value of f here is 3.9×10^{-23} versus 1.3×10^{-26} in Section 4.4.) The quantities d_l in Table 3 are the number of timesteps between mile-markers where the energy and plots of the solution were recorded. In this case, we recorded 60 slices of the solution between $t = 0$ and $t = T/4$. The running times in the right panel of Figure 20 report the time to advance from one mile-marker to the next. It was not possible to solve this problem via the ACM method or MINPACK, so this test compares running times of the trust region method on several machines. In quadruple precision, we evolved the solution but did not compute the Jacobian. Two of the jobs on the cluster (1 node and 2 nodes) were terminated early due to insufficient available wall-clock time. When using the GPU, there is little improvement in performance in also running openMP on the CPU. For example, switching from 12 threads (shown in the figure) to one thread (not shown) slows the computation of the Jacobian by about 10 percent, but speeds up the computation of the solution by about 1 percent. When evolving the solution on a large problem, the GPU is fully utilized; however, when evolving the Jacobian, the GPU is idle about 60 percent of the time. Thus, we can run 2-3 jobs simultaneously to improve the effective performance of the GPU by another factor of 2 over what is plotted in the figures. This is also true of the Lawrenceium cluster — while using more nodes to solve a single problem stops paying off around 8 nodes, we can run multiple jobs independently. Most of the large-amplitude solutions in Figure 10 were computed in this way on the Lawrenceium cluster, before we acquired the GPU device.

5. Conclusion

We have shown how to compute time-periodic solutions of the free-surface Euler equations with improved resolution, accuracy and robustness by formulating the shooting method as an overdetermined nonlinear least squares problem and exploiting parallelism in the Jacobian calculation. This made it possible to resolve a long-standing open

question, posed by Penney and Price in 1952, on whether the most extreme standing wave develops wave crests with sharp 90 degree corners each time the fluid comes to rest. Previous numerical studies reached different conclusions about the form of the limiting wave, but none were able to resolve the fine-scale oscillations that develop due to resonant effects. While we cannot say for certain that no standing wave exists that forms sharp corners at periodic time-intervals, we can say that such a wave does not lie at the end of a family of increasingly sharp standing waves parametrized by crest acceleration, A_c . Indeed, crest acceleration is not a monotonic function, and the bifurcation curve becomes fragmented as $A_c \rightarrow 1$, with different branches corresponding to different fine-scale oscillation patterns that emerge at the surface of the wave. Following any of these branches in either direction leads to increasingly oscillatory solutions with curvature that appears to blow up throughout the interval $[0, 2\pi]$, not just at the crest tip.

Small-amplitude standing waves have been proved to exist in finite depth by Plotnikov and Toland [24], and in infinite depth by Plotnikov, Toland and Iooss [20]. However, the proofs rely on a Nash-Moser iteration that only guarantees existence for values of the amplitude in a totally disconnected Cantor set [25, 26]. In shallow water, with $h = 0.05$, we do see evidence that solutions do not come in smooth families. For example, in Figure 15, the number of visible disconnections in the bifurcation diagrams increases dramatically from $\hat{\varphi}_1(0)$ to $\hat{\varphi}_{17}(0)$ to $\hat{\eta}_{36}(0)$. There are also a few gaps along the T -axis where the numerical method failed to find a solution, i.e. the minimum value of f did not decrease below the target of 10^{-26} regardless of how many additional Fourier modes were included in the simulation. It is easy to imagine that removing all the gaps that arise in this fashion as the mesh is refined and the numerical precision is increased could lead to a Cantor-like set of allowed periods.

Our numerical method measures success by how small the objective function f and residual r become. It will succeed if it can find initial conditions that are close enough to those of an exactly time-periodic solution, or at least of a solution that is time-periodic up to roundoff error tolerances. For the residual to be small, the bifurcation parameter must nearly belong to the Cantor set of allowed values, but membership need not be exact. If the Cantor set is fat enough (i.e. has nearly full measure), then most values of the bifurcation parameter will be close to some element of the set — roundoff error fills in the smallest gaps. While it is possible that our numerical method would report a false positive, this seems unlikely. The residuals of our solutions are not under-predicted by the minimization algorithm due to formulation of the problem as an overdetermined system. Indeed, we saw in Figure 14 that f decreases from 1.3×10^{-26} to 8.6×10^{-27} for solution O when the initial conditions are evolved on a finer mesh in quadruple precision, and decreases from 1.9×10^{-28} to 2.1×10^{-60} for solution A when the minimization is repeated in quadruple precision. This latter test is particularly convincing that the method is converging to an exactly time-periodic solution.

If standing waves on water of infinite depth do not come in smooth families, as suggested by the analysis of [20], they are remarkably well approximated by them. Prior to our work, no numerical evidence of disconnections in the bifurcation curves had been observed. Wilkening [17] found several disconnections for values of crest acceleration $A_c > 0.99$, but none at smaller values. As shown in Figure 21, there is one additional disconnection around $A_c = 0.947$ that can be observed in double-precision that was missed in [17]. However, the points at which resonance is supposed

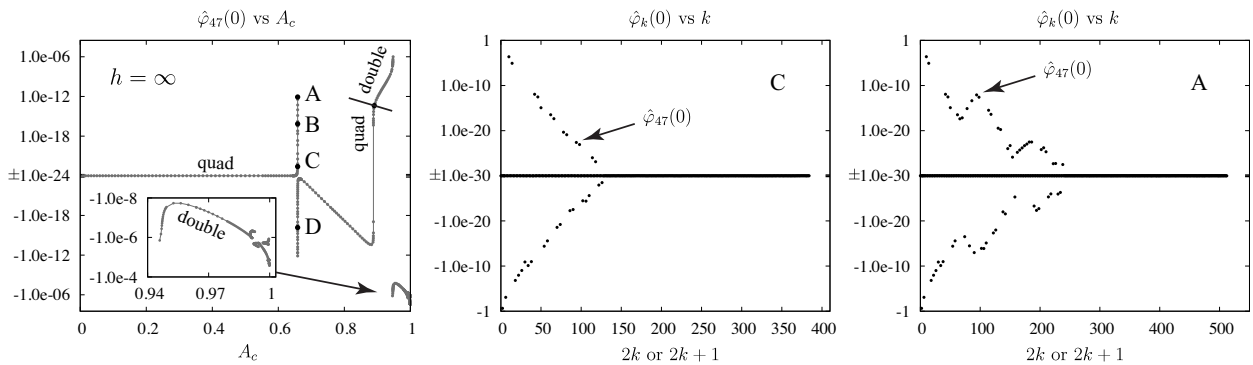


Figure 21: Study of resonance in deep water standing waves. (left) Switching from double- to quadruple-precision arithmetic reveals only one additional disconnection in the bifurcation curves. The inset graph shows how the disconnections of Figure 10 look when c_{47} is plotted rather than c_1 , c_5 and c_{60} . Solutions B and D are the points where $|c_{47}/c_1| \approx 3 \times 10^{-16}$, just barely above the roundoff threshold. The gap in crest acceleration between these solutions is $A_c(D) - A_c(B) = 1.4 \times 10^{-9}$; thus, it is extremely unlikely in a parameter study that one would land in this gap. Outside of this gap, resonant effects from this disconnection are smaller than the roundoff threshold. (center and right) Resonance causes bursts of growth in the Fourier spectrum, but the modes continue to decay exponentially in the long run.

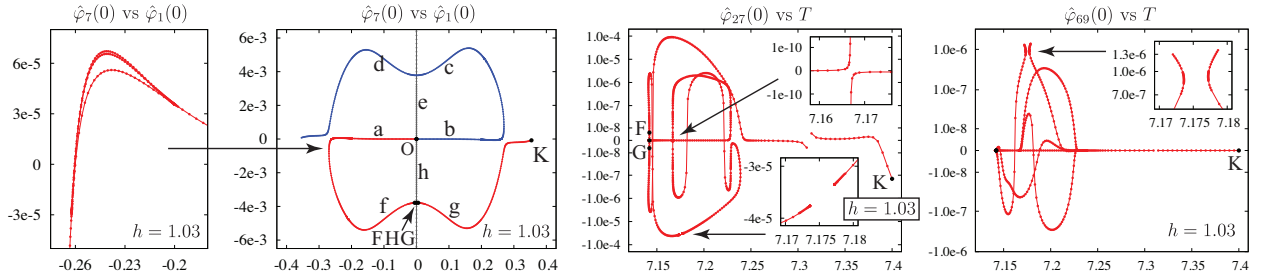


Figure 22: A closer look at the bifurcation structure in Figure 7 in the $h = 1.03$ case reveals a number of additional side-branches that trace back and forth over nearly the same curves when low-frequency modes are plotted (left), but become well-separated when high frequency modes are plotted (right center, right). A small gap near $T = 7.175$ has formed on one of the wings in the plots of $\hat{\varphi}_{27}(0)$ and $\hat{\varphi}_{69}(0)$ vs T .

to cause difficulty are expected to be dense over the whole range $0 < A_c < 1$. We re-computed the solutions up to $A_c = 0.8907$ in quadruple precision, expecting several new disconnections to emerge in high-frequency Fourier modes. Surprisingly, we could only find one, at $A_c = 0.658621$. Using a bisection algorithm to zoom in on the disconnection in the 47th Fourier mode from both sides (using c_5 as the bifurcation parameter), we were able to extend the side branches from $c_{47} \approx \pm 10^{-27}$ to $c_{47} \approx \pm 10^{-12}$. These side branches become observable in double-precision at points B and D in Figure 21. However, the gap in crest acceleration between solutions B and D is only 1.4×10^{-9} units wide. Thus, it is extremely unlikely that this resonance could be detected in double-precision without knowing where to look. Presumably the same issue prevents us from seeing additional disconnections in quadruple-precision. This suggests that the Cantor-like set of allowed values of the amplitude parameter is very fat, with gaps decaying to zero rapidly with the wave number of the resonant mode.

In finite depth, with $h \approx 1$, a connection can be seen between resonance and non-uniqueness of solutions. The main difference from the $h = 0.05$ and $h = \infty$ cases is that for $h \approx 1$, the disconnections lead to side-branches that can be tracked a great distance via numerical continuation, and are often found to be globally connected to one another. Traversing these side branches causes high-frequency modes to sweep out small-amplitude loop-shaped structures. These loops are “long and thin” in the sense that low-frequency modes trace back over the previously swept out bifurcation curves while traversing the loop, with little deviation in the lateral direction. For example, in Figure 22, the 27th Fourier mode executes a number of excursions in which it grows to around 10^{-6} , causing the period and first Fourier modes to sweep back and forth over much larger ranges, $7.167 < T < 7.229$ and $-0.200 > \hat{\varphi}_1(0) > -0.262$. These loops are plotted in Figures 7 and 9 as well, but the curves are indistinguishable from one another at this resolution since the lateral deviations are so small. Looking at the third panel of Figure 22, one might ask, “how many solutions are there with period $T = 7.2$.” If we had not noticed any of the disconnections (note the exponential scaling of the axis), we would have answered 1. If we had only tracked the outer wings, we would have answered 3. Having tracked all the branches shown, the answer appears to be 5. But of course there are probably infinitely many disconnections in higher-frequency Fourier modes that we did not resolve or track, and some of these may lead to additional solutions with $T = 1.2$. Physically, all these crossings of $T = 1.2$ correspond to a hierarchy of “standing waves on standing waves,” with different mode amplitudes and phases working together to create a globally time-periodic solution with this period. The fact that the low-frequency bifurcation curves sweep back and forth over nearly the same graph reinforces the physically reasonable idea that high-frequency, low amplitude waves oscillating on the surface of low-frequency, large amplitude waves will not significantly change the large-scale behavior.

In summary, time-periodic water waves occur in abundance in numerical simulations, and appear to be highly non-unique, partly due to the Wilton’s ripple phenomenon of mixed-mode solutions co-existing with pure-mode solutions near a degenerate bifurcation, and also due to a tendency of the bifurcation curves to fold back on themselves each time a resonant mode is excited. Proofs of existence based on Nash-Moser iteration must somehow select among these multiple solutions, and it would be interesting to know whether the Cantor-like structure in the analysis is caused by a true lack of existence for parameter values outside of this set, or is partly caused by non-uniqueness. Finally, we note that most of the disconnections in the numerically computed bifurcation curves disappear in the infinite depth limit, and remarkably small residuals can be achieved with smooth families of approximate solutions. This calls for further investigation of the extent to which the obstacles to proving smooth dependence of solutions on amplitude can be overcome or quantified.

Acknowledgments

This research was supported in part by the Director, Office of Science, Computational and Technology Research, U.S. Department of Energy under Contract No. DE-AC02-05CH11231, and by the National Science Foundation through grant DMS-0955078. Some of the computations were performed on the Lawrence Livermore supercluster at LBNL.

A. Boundary integral formulation

While many numerical methods exist to evolve irrotational flow problems [43, 44, 45, 2, 88, 49, 37, 51, 53, 46], we have found that a direct boundary integral implementation of (2.1) is the simplest and most effective approach for problems where η remains single valued, i.e. the interface does not overturn. Suppressing t in the notation, we represent the complex velocity potential $\Phi(z) = \phi(z) + i\psi(z)$ as a Cauchy integral [89]

$$\Phi(z) = \frac{1}{2\pi i} PV \int_{-\infty}^{\infty} \frac{-\zeta'(\alpha)}{\zeta(\alpha) - z} \mu(\alpha) d\alpha, \quad \zeta(\alpha) = \xi(\alpha) + i\eta(\xi(\alpha)), \quad (\text{A.1})$$

where z is a field point in the fluid, $\mu(\alpha)$ is the (real-valued) dipole density, $\zeta(\alpha)$ parametrizes the free surface, PV indicates a principal value integral, $\eta(x)$ retains its meaning from equation (2.1), and the change of variables $x = \xi(\alpha)$ will be used to smoothly refine the mesh in regions of high curvature. The minus sign in (A.1) accounts for the fact that Cauchy integrals are usually parametrized counter-clockwise, but we have parametrized the curve so the fluid region lies to the right of $\zeta(\alpha)$. When the fluid depth is finite, we impose the tangential flow condition using an identical double-layer potential on the mirror image surface, $\bar{\zeta}(\alpha)$. This assumes we have set $h = 0$ in (2.3), absorbing the mean fluid depth into η itself. We also use $\frac{1}{2} \cot \frac{\alpha}{2} = PV \sum_k \frac{1}{z + 2\pi k}$ to sum (A.1) over periodic images. The result is

$$\Phi(z) = \frac{1}{2\pi i} \int_0^{2\pi} \left[\frac{\zeta'(\alpha)}{2} \cot \left(\frac{z - \zeta(\alpha)}{2} \right) - \frac{\bar{\zeta}'(\alpha)}{2} \cot \left(\frac{z - \bar{\zeta}(\alpha)}{2} \right) \right] \mu(\alpha) d\alpha. \quad (\text{A.2})$$

Note that Φ is real-valued on the x -axis, indicating that the stream function ψ is zero (and therefore constant) along the bottom boundary.

As z approaches $\zeta(\alpha)$ from above (+) or below (-), the Plemelj formula [89] gives

$$\Phi(\zeta(\alpha)^\pm) = \mp \frac{1}{2} \mu(\alpha) + \frac{PV}{2\pi i} \int_0^{2\pi} \left[\frac{\zeta'(\beta)}{2} \cot \frac{\zeta(\alpha) - \zeta(\beta)}{2} - \frac{\bar{\zeta}'(\beta)}{2} \cot \frac{\zeta(\alpha) - \bar{\zeta}(\beta)}{2} \right] \mu(\beta) d\beta. \quad (\text{A.3})$$

We regularize the principal value integral by subtracting and adding $\frac{1}{2} \cot \left(\frac{\alpha - \beta}{2} \right)$ from the first term in brackets [90, 91, 50]. The result is

$$\Phi(\zeta(\alpha)^\pm) = \mp \frac{1}{2} \mu(\alpha) - \frac{i}{2} H\mu(\alpha) + \frac{1}{2\pi i} \int_0^{2\pi} [\tilde{K}_1(\alpha, \beta) + \tilde{K}_2(\alpha, \beta)] \mu(\beta) d\beta, \quad (\text{A.4})$$

where $Hf(\alpha) = \frac{1}{\pi} PV \int_{-\infty}^{\infty} \frac{f(\beta)}{\alpha - \beta} d\alpha = \frac{1}{\pi} PV \int_0^{2\pi} \frac{f(\beta)}{2} \cot \left(\frac{\alpha - \beta}{2} \right) d\beta$ is the Hilbert transform and

$$\tilde{K}_1(\alpha, \beta) = \frac{\zeta'(\beta)}{2} \cot \frac{\zeta(\alpha) - \zeta(\beta)}{2} - \frac{1}{2} \cot \frac{\alpha - \beta}{2}, \quad \tilde{K}_2(\alpha, \beta) = \frac{\bar{\zeta}'(\beta)}{2} \cot \frac{\zeta(\alpha) - \bar{\zeta}(\beta)}{2}. \quad (\text{A.5})$$

We note that $\tilde{K}_1(\alpha, \beta)$ is continuous at $\beta = \alpha$ if we define $\tilde{K}_1(\alpha, \alpha) = -\zeta''(\alpha)/[2\zeta'(\alpha)]$. Taking the real part of (A.4) at $z = \zeta(\alpha)^-$ yields a second-kind Fredholm integral equation for $\mu(\alpha)$ in terms of $\varphi(\xi(\alpha))$,

$$\frac{1}{2} \mu(\alpha) + \frac{1}{2\pi} \int_0^{2\pi} [K_1(\alpha, \beta) + K_2(\alpha, \beta)] \mu(\beta) d\beta = \varphi(\xi(\alpha)), \quad (\text{A.6})$$

where $K_j(\alpha, \beta) = \text{Im}\{\tilde{K}_j(\alpha, \beta)\}$. Once $\mu(\alpha)$ is known, it follows from (A.2) that

$$\Phi'(z) = u(z) - iv(z) = \frac{1}{2\pi i} \int_0^{2\pi} \left[\frac{1}{2} \cot \left(\frac{z - \zeta(\alpha)}{2} \right) - \frac{1}{2} \cot \left(\frac{z - \bar{\zeta}(\alpha)}{2} \right) \right] \gamma(\alpha) d\alpha, \quad (\text{A.7})$$

where $\gamma(\alpha) = \mu'(\alpha)$ is the (normalized) vortex sheet strength. As z approaches $\zeta(\alpha)$ from above or below, one may show [41] that

$$\zeta'(\alpha)\Phi'(\zeta(\alpha)^\pm) = \mp \frac{1}{2}\gamma(\alpha) + \frac{PV}{2\pi i} \int_0^{2\pi} \left[\frac{\zeta'(\alpha)}{2} \cot \frac{\zeta(\alpha) - \zeta(\beta)}{2} - \frac{\zeta'(\alpha)}{2} \cot \frac{\zeta(\alpha) - \bar{\zeta}(\beta)}{2} \right] \gamma(\beta) d\beta. \quad (\text{A.8})$$

Note that ζ' is evaluated at β in (A.3) and at α in (A.8) inside the integral. We regularize the principal value integral using the same technique as before to obtain

$$\zeta'(\alpha)\Phi'(\zeta(\alpha)^\pm) = \mp \frac{1}{2}\gamma(\alpha) - \frac{i}{2}H\gamma(\alpha) + \frac{1}{2\pi i} \int_0^{2\pi} [\widetilde{G}_1(\alpha, \beta) + \widetilde{G}_2(\alpha, \beta)] \gamma(\beta) d\beta, \quad (\text{A.9})$$

where

$$\widetilde{G}_1(\alpha, \beta) = \frac{\zeta'(\alpha)}{2} \cot \frac{\zeta(\alpha) - \zeta(\beta)}{2} - \frac{1}{2} \cot \frac{\alpha - \beta}{2}, \quad \widetilde{G}_2(\alpha, \beta) = \frac{\zeta'(\alpha)}{2} \cot \frac{\zeta(\alpha) - \bar{\zeta}(\beta)}{2}. \quad (\text{A.10})$$

$\widetilde{G}_1(\alpha, \beta)$ is continuous at $\beta = \alpha$ if we define $\widetilde{G}_1(\alpha, \alpha) = \zeta''(\alpha)/[2\zeta'(\alpha)]$. We could read off $u = \phi_x$ and $v = \phi_y$ from (A.9) for use in the right hand side of (2.1). Instead, as an intermediate step, we compute the output of the Dirichlet-Neumann operator defined in (2.6),

$$\begin{aligned} |\zeta'(\alpha)|\mathcal{G}\varphi(\zeta(\alpha)) &= |\zeta'(\alpha)| \frac{\partial \phi}{\partial n}(\zeta(\alpha)) = \lim_{z \rightarrow \zeta(\alpha)^-} \text{Re} \{ i\zeta'(\alpha)[u(z) - iv(z)] \} \\ &= \frac{1}{2}H\gamma(\alpha) + \frac{1}{2\pi} \int_0^{2\pi} [G_1(\alpha, \beta) + G_2(\alpha, \beta)] \gamma(\beta) d\beta. \end{aligned} \quad (\text{A.11})$$

Here $G_j(\alpha, \beta) = \text{Re}\{\widetilde{G}_j(\alpha, \beta)\}$ and $i\zeta'(\alpha)/|\zeta'(\alpha)|$ represents the normal vector to the curve. Note that the dot product of two complex numbers z and w (thought of as vectors in \mathbb{R}^2) is $\text{Re}\{z\bar{w}\}$. Once $\mathcal{G}\varphi(x)$ is known, we can evaluate the right hand side of (2.1) using (2.9).

For visualization, it is often useful to evaluate the velocity and pressure inside the fluid. The velocity was already given in terms of the vortex sheet strength in (A.7) above. For pressure, we use the unsteady Bernoulli equation

$$\phi_t + \frac{1}{2}|\nabla\phi|^2 + gy + \frac{p}{\rho} = c(t), \quad (\text{A.12})$$

where $c(t)$ was given in (2.4). One option for computing ϕ_t is to differentiate (A.6) with respect to time to obtain an integral equation for μ_t (see [92]), then express ϕ_t in terms of μ_t by differentiating (A.2). A simpler approach is to differentiate the Laplace equation (2.3) with respect to time. The value of ϕ_t on the upper boundary is $\varphi_t - \phi_y\eta_t$, which is known. Since the real part of (A.2) gives the solution $\phi(z)$ of Laplace's equation with boundary condition φ on the upper surface, we can replace φ with $\varphi_t - \phi_y\eta_t$ in (A.6) to convert (A.2) into a formula for $\phi_t(z)$ instead.

B. Linearized and adjoint equations for the water wave

In this section we derive explicit formulas for the variational and adjoint equations of Sections 3.2 and 3.3. A dot will be used to denote a directional derivative with respect to the initial conditions. The equation $\dot{q}_t = DF(q)\dot{q}$ of (3.23) is simply

$$\dot{\eta}(x, 0) = \dot{\eta}_0(x), \quad \dot{\psi}(x, 0) = \dot{\psi}_0(x), \quad t = 0, \quad (\text{B.1a})$$

$$\dot{\phi}_{xx} + \dot{\phi}_{yy} = 0, \quad -h < y < \eta, \quad (\text{B.1b})$$

$$\dot{\phi}_y = 0, \quad y = -h, \quad (\text{B.1c})$$

$$\dot{\phi} + \phi_y\dot{\eta} = \dot{\psi}, \quad y = \eta, \quad (\text{B.1d})$$

$$\dot{\eta}_t + \dot{\eta}_x\phi_x + \eta_x\dot{\phi}_x + \eta_x\phi_{xy}\dot{\eta} = \dot{\phi}_y + \phi_{yy}\dot{\eta}, \quad y = \eta, \quad (\text{B.1e})$$

$$\dot{\phi}_t = P \left[- \left(\eta_x\phi_x\phi_y + \frac{1}{2}\phi_x^2 - \frac{1}{2}\phi_y^2 \right) - g\dot{\eta} + \frac{\sigma}{\rho} \partial_x \left(\frac{\dot{\eta}_x}{(1 + \eta_x^2)^{3/2}} \right) \right], \quad y = \eta. \quad (\text{B.1f})$$

Note that evaluation of $\dot{\phi}(x, y, t)$ on the free surface gives $[\dot{\phi}(x) - \phi_y(x, \eta(x), t)\dot{\eta}(x)]$ rather than $\dot{\phi}(x)$ due to the boundary perturbation. Making use of $\phi_{yy} = -\phi_{xx}$, (B.1e) can be simplified to

$$\dot{\eta}_t = (\dot{\phi}_y - \eta_x \dot{\phi}_x) - (\dot{\eta} \phi_x)', \quad (\text{B.2})$$

where a prime indicates an x -derivative along the free surface, e.g. $f' := \frac{d}{dx}f(x, \eta(x), t) = f_x + \eta_x f_y$. Equation (B.1f) may also be simplified, using

$$\begin{aligned} \left(\eta_x \phi_x \phi_y + \frac{1}{2} \phi_x^2 - \frac{1}{2} \phi_y^2 \right)' &= \dot{\eta}_x \phi_x \phi_y + \eta_x \dot{\phi}_x \phi_y + \eta_x \phi_{xy} \dot{\eta} \phi_y + \eta_x \phi_x \dot{\phi}_y + \eta_x \phi_x \phi_{yy} \dot{\eta} + \phi_x \dot{\phi}_x + \phi_x \phi_{xy} \dot{\eta} - \phi_y \dot{\phi}_y - \phi_y \phi_{yy} \dot{\eta} \\ &= (\dot{\eta} \phi_x \phi_y)' + \phi_x \dot{\phi}' - \phi_y (\dot{\phi}_y - \eta_x \dot{\phi}_x). \end{aligned} \quad (\text{B.3})$$

The equation $\tilde{q}_s = DF(q) * \tilde{q}$ is obtained from

$$\begin{aligned} \langle \dot{q}, \tilde{q}_s \rangle = \langle \dot{q}_t, \tilde{q} \rangle &= \frac{1}{2\pi} \int_0^{2\pi} \left[\underline{(\dot{\phi}_y - \eta_x \dot{\phi}_x)} - (\dot{\eta} \phi_x)' \right] \tilde{\eta} dx \\ &+ \frac{1}{2\pi} \int_0^{2\pi} P \left[-(\dot{\eta} \phi_x \phi_y)' - \phi_x \dot{\phi}' + \phi_y \underline{(\dot{\phi}_y - \eta_x \dot{\phi}_x)} - g\dot{\eta} + \frac{\sigma}{\rho} \partial_x \left(\frac{\dot{\eta}_x}{(1 + \eta_x^2)^{3/2}} \right) \right] \tilde{\varphi} dx. \end{aligned} \quad (\text{B.4})$$

The right-hand side must now be re-organized so we can identify \tilde{q}_s . P is self-adjoint, so it can be transferred from the bracketed term to $\tilde{\varphi}$. The underlined terms may be written $\mathcal{G}\dot{\phi}$, where $\dot{\phi}$ is evaluated on the free surface. Green's identity shows that \mathcal{G} is self-adjoint. Indeed, if $\dot{\phi}$ and χ satisfy Laplace's equation with Neumann conditions on the bottom boundary, then

$$0 = \iint (\chi \Delta \dot{\phi} - \dot{\phi} \Delta \chi) dA = \int \chi \frac{\partial \dot{\phi}}{\partial n} - \dot{\phi} \frac{\partial \chi}{\partial n} ds = \int \chi \mathcal{G} \dot{\phi} dx - \int \dot{\phi} \mathcal{G} \chi dx. \quad (\text{B.5})$$

Thus, from (B.4), we obtain

$$\langle \dot{q}, \tilde{q}_s \rangle = \frac{1}{2\pi} \int_0^{2\pi} \left[\dot{\phi} \mathcal{G} \chi + \dot{\eta} \phi_x \tilde{\eta}' + \dot{\eta} \phi_x \phi_y (P\tilde{\varphi})' + \dot{\phi} (\phi_x P\tilde{\varphi})' - g\dot{\eta} P\tilde{\varphi} + \frac{\sigma}{\rho} \dot{\eta} \partial_x \left(\frac{\tilde{\varphi}_x}{(1 + \eta_x^2)^{3/2}} \right) \right] dx,$$

where χ is an auxiliary solution of Laplace's equation defined to be $(\tilde{\eta} + \phi_y P\tilde{\varphi})$ on the free surface. Finally, we substitute $\dot{\phi} = \dot{\phi} - \phi_y \dot{\eta}$ and match terms to arrive at the adjoint system

$$\tilde{\eta}(x, 0) = 0, \quad \tilde{\varphi}(x, 0) = \varphi(x, T/4), \quad s = 0, \quad (\text{B.6a})$$

$$\chi_{xx} + \chi_{yy} = 0, \quad -h < y < \eta, \quad (\text{B.6b})$$

$$\chi_y = 0, \quad y = -h, \quad (\text{B.6c})$$

$$\chi = \tilde{\eta} + \phi_y P\tilde{\varphi}, \quad y = \eta, \quad (\text{B.6d})$$

$$\tilde{\varphi}_s = (\chi_y - \eta_x \chi_x) + (\phi_x P\tilde{\varphi})', \quad y = \eta, \quad (\text{B.6e})$$

$$\tilde{\eta}_s = -\phi_y (\chi_y - \eta_x \chi_x) + \phi_x \tilde{\eta}_x - \phi_y \phi_x' P\tilde{\varphi} - gP\tilde{\varphi} + \frac{\sigma}{\rho} \partial_x \left(\frac{\tilde{\varphi}_x}{(1 + \eta_x^2)^{3/2}} \right), \quad y = \eta. \quad (\text{B.6f})$$

The initial conditions (B.6a) are specific to the objective function (3.21), but are easily modified to handle the alternative objective function (3.18). Note that the adjoint problem has the same structure as the forward and linearized problems, with a Dirichlet to Neumann map appearing in the evolution equations for $\tilde{\eta}$ and $\tilde{\varphi}$. We use the boundary integral method described in Appendix A to compute $\mathcal{G}\chi$, and employ a dense output formula to interpolate η and φ between timesteps at intermediate Runge-Kutta stages of the adjoint problem, as explained in Section 3.2.

C. Levenberg-Marquardt implementation with delayed Jacobian updates

Since minimizing f in (3.17) is a small-residual nonlinear least squares problem, the Levenberg-Marquardt method [40] is quadratically convergent. Our goal in this section is to discuss modifications of the algorithm in which re-computation of the Jacobian is delayed until the previously computed Jacobian ceases to be useful. By appropriately

adjusting the step size in the numerical continuation algorithm, it is usually only necessary to compute the Jacobian once per solution. Briefly, the Levenberg-Marquardt method works by minimizing the quadratic function

$$f_{\text{approx}}(p) = f(c) + g^T p + \frac{1}{2} p^T B p, \quad g = \nabla f(c) = J^T(c)r(c), \quad B = J(c)^T J(c) \quad (\text{C.1})$$

over the trust region $\|p\| \leq \Delta$. The true Hessian of f at c satisfies $H - B = \sum_i r_i \nabla^2 r_i$, which is small if r is small. The solution of this constrained quadratic minimization problem is the same as the solution of a linear least-squares problem with an unknown parameter λ :

$$\min_p \left\| \begin{pmatrix} J \\ \sqrt{\lambda} I \end{pmatrix} p + \begin{pmatrix} r \\ 0 \end{pmatrix} \right\|, \quad \lambda \geq 0, \quad (\|p\| - \Delta)\lambda = 0. \quad (\text{C.2})$$

Formulating the problem this way (instead of solving $(B + \lambda I)p = -g$) avoids squaring the condition number of J . Rather than use the MINPACK algorithm [40] to find the Lagrange multiplier λ , we compute the (thin) SVD of J , and define

$$J = USV^T, \quad S = \text{diag}\{\sigma\}, \quad \tilde{p} = V^T p, \quad \tilde{r} = U^T r, \quad \tilde{g} = S^T \tilde{r}. \quad (\text{C.3})$$

Here U is $m \times n$ and $S = S^T$ is $n \times n$. This leads to an equivalent problem

$$\min_{\tilde{p}} \left\| \begin{pmatrix} S \\ \sqrt{\lambda} I \end{pmatrix} \tilde{p} + \begin{pmatrix} \tilde{r} \\ 0 \end{pmatrix} \right\|, \quad \lambda \geq 0, \quad (\|\tilde{p}\| - \Delta)\lambda = 0, \quad (\text{C.4})$$

which can be solved in $O(n)$ time by performing a Newton iteration on $\tau(\lambda)$, defined as

$$\tau(\lambda) = \frac{1}{\|\tilde{p}\|} - \frac{1}{\Delta}, \quad \tilde{p} = \arg \min_{\tilde{p}} \left\| \begin{pmatrix} S \\ \sqrt{\lambda} I \end{pmatrix} \tilde{p} + \begin{pmatrix} \tilde{r} \\ 0 \end{pmatrix} \right\|. \quad (\text{C.5})$$

It is easy to show that τ is an increasing, concave down function for $\lambda \geq 0$ (assuming S is non-singular); thus, if $\tau(0) < 0$, the Newton iteration starting at $\lambda^{(0)} = 0$ will increase monotonically to the solution of (C.4) with $\tau(\lambda^{(l)})$ increasing to zero. This Newton iteration is equivalent to

$$\begin{aligned}
& l = 0, \quad \lambda^{(0)} = 0, \quad \tilde{p}_0 = \arg \min_{\tilde{p}} \|S \tilde{p} + \tilde{r}\| \\
& \mathbf{while} \left(\frac{\|\tilde{p}_l\| - \Delta}{\Delta} \right) > \text{tol} \\
& \quad \lambda^{(l+1)} = \lambda^{(l)} + \frac{\tilde{p}_l^T \tilde{p}_l}{\tilde{p}_l^T (S^T S + \lambda^{(l)} I) \tilde{p}_l} \left(\frac{\|\tilde{p}_l\| - \Delta}{\Delta} \right) \\
& \quad l = l + 1 \\
& \quad \tilde{p}_l = \arg \min_{\tilde{p}} \left\| \begin{pmatrix} S \\ \sqrt{\lambda^{(l)}} I \end{pmatrix} \tilde{p} + \begin{pmatrix} \tilde{r} \\ 0 \end{pmatrix} \right\| \\
& \mathbf{end}
\end{aligned}$$

We use $\text{tol} = 10^{-12}$ in double-precision and 10^{-24} in quadruple precision. It is not critical that λ be computed to such high accuracy, but as the Newton iteration is inexpensive once the SVD of J is known, there is no reason not to iterate to convergence. At the end, we set $p = V\tilde{p}$.

We remark that it is more common to compute λ by a sequence of QR factorizations of $[J; \sqrt{\lambda^{(l)}} I]$, as is done in MINPACK. However, the SVD approach is simpler, and similar in speed, since several QR factorizations have to be performed to compute λ while only one SVD must be computed. Moreover, we can re-use J several times instead of re-computing it each time a step is accepted. When this is done, it pays to have factored $J = USV^T$ up front.

Delaying the computation of J requires a modified strategy for updating the trust region radius, as well as a means of deciding when the minimization is complete, and when to re-compute J . Our design decisions are summarized as follows:

1. The algorithm terminates if $f = 0$, or if c is unchanged from the previous iteration (i.e. $c + p$ equals c in floating point arithmetic), or if the algorithm reaches the *roundoff_regime* phase, and then a step is rejected or *stepsJ* reaches *max_stepsJ*. Here *stepsJ* counts accepted steps since J was last evaluated, and the *roundoff_regime* phase

begins if $f < f_{\text{tol}}$ or $\Delta < g_{\text{tol}}$, where the tolerances and $\text{max_steps}J$ are specified by the user. If the Jacobian has just been computed (i.e. $\text{steps}J = 0$), we also check if $\|g\| < g_{\text{tol}}$ or $|df|/f < df_{\text{tol}}$ to trigger *roundoff_regime*. Here $df = f_{\text{approx}}(c + p) - f(c)$ is the predicted change in f when minimizing the quadratic model f_{approx} over the trust region, and df_{tol} is specified by the user. We used

$$f_{\text{tol}} = 10^{-26}, \quad g_{\text{tol}} = 10^{-13}, \quad \text{max_steps}J = 10, \quad df_{\text{tol}} = 10^{-5}.$$

The idea of *roundoff_regime* is to try to improve f through a few additional residual calculations without recomputing J .

2. Steps are accepted if $\rho = [f(c + p) - f(c)]/df > 0$; otherwise they are rejected. Note that ρ is the ratio of the actual change to the predicted change, the latter being negative. We also use ρ to adjust Δ . If $\rho < \rho_0 = 1/4$, we replace Δ by $\|p\|$ times $\alpha_0 = 3/8$. If $\rho > \rho_1 = 0.85$ and $\|p\| > 0.9\Delta$, we multiply Δ by $\alpha_1 = 1.875$. Otherwise we leave Δ alone. So far this agrees with the standard trust region mechanism [40] for adjusting Δ , with slightly different parameters. What we do differently is define a parameter *delta_trigger* to be a prescribed fraction, namely $\alpha_2 = 0.2$, of *delta_first_rejected*, the first rejected radius after (or coinciding with) an accepted step. Note that the radius is rejected ($\rho < \rho_0$), not necessarily the step ($\rho \leq 0$). The reason to wait for an accepted step is to let the trust region shrink normally several times in a row if the Jacobian is freshly computed ($\text{steps}J = 0$).

3. The Jacobian is re-computed if *roundoff_regime* has not occurred, and either $\text{steps}J$ reaches $\text{max_steps}J$, or $\text{steps}J > 0$ and Δ drops below *delta_trigger*, or $\text{steps}J > 0$ and $|df|/f < df_{\text{tol}}$. This last test avoids iterating on an old Jacobian if the new residual is nearly orthogonal to its columns — there is little point in continuing if f_{approx} cannot be decreased significantly. The parameters α_i were chosen so that

$$\max(\alpha_0^2, \alpha_0^3 \alpha_1^2) < \alpha_2 < \min(\alpha_0, \alpha_0^2 \alpha_1), \quad (\text{C.6})$$

which triggers the re-computation of J if two radii are rejected in a row, or on a reject-accept-reject-accept-reject sequence, assuming $\|p\| = \Delta$ on each rejection. Before computing J , if *delta_first_rejected* has been defined since J was last computed, we reset Δ to

$$\Delta = \text{delta_first_rejected}/\alpha_1.$$

This makes up for the decreases in Δ that occur due to using an old Jacobian.

4. We compute r but not J if a step is rejected on a freshly computed Jacobian, or if a step is accepted or rejected without triggering one of the conditions mentioned above for computing J .

References

- [1] L. W. Schwartz, A. K. Whitney, A semi-analytic solution for nonlinear standing waves in deep water, *J. Fluid Mech.* 107 (1981) 147–171.
- [2] G. N. Mercer, A. J. Roberts, Standing waves in deep water: Their stability and extreme form, *Phys. Fluids A* 4 (2) (1992) 259–269.
- [3] G. N. Mercer, A. J. Roberts, The form of standing waves on finite depth water, *Wave Motion* 19 (1994) 233–244.
- [4] D. H. Smith, A. J. Roberts, Branching behavior of standing waves — the signatures of resonance, *Phys. Fluids* 11 (1999) 1051–1064.
- [5] C. P. Tsai, D. S. Jeng, Numerical Fourier solutions of standing waves in finite water depth, *Appl. Ocean Res.* 16 (1994) 185–193.
- [6] P. J. Bryant, M. Stiassnie, Different forms for nonlinear standing waves in deep water, *J. Fluid Mech.* 272 (1994) 135–156.
- [7] W. W. Schultz, J. M. Vanden-Broeck, L. Jiang, M. Perlin, Highly nonlinear standing water waves with small capillary effect, *J. Fluid Mech.* 369 (1998) 253–272.
- [8] M. Okamura, Standing gravity waves of large amplitude on deep water, *Wave Motion* 37 (2003) 173–182.
- [9] A. J. Roberts, Highly nonlinear short-crested water waves, *J. Fluid Mech.* 135 (1983) 301–321.

- [10] T. R. Marchant, A. J. Roberts, Properties of short-crested waves in water of finite depth, *J. Austral. Math. Soc. B* 29 (1987) 103–125.
- [11] T. J. Bridges, F. Dias, D. Menasce, Steady three-dimensional water-wave patterns on finite-depth fluid, *J. Fluid Mech.* 436 (2001) 145–175.
- [12] M. Ioualalen, M. Okamura, S. Cornier, C. Kharif, A. J. Roberts, Computation of short-crested deep-water waves, *J. Waterway, Port, Coast and Ocean Engrg* 132 (3) (2006) 157–165.
- [13] W. G. Penney, A. T. Price, Finite periodic stationary gravity waves in a perfect liquid, part II, *Phil. Trans. R. Soc. London A* 244 (1952) 254–284.
- [14] G. I. Taylor, An experimental study of standing waves, *Proc. Roy. Soc. A* 218 (1953) 44–59.
- [15] M. A. Grant, Standing Stokes waves of maximum height, *J. Fluid Mech.* 60 (1973) 593–604.
- [16] M. Okamura, On the enclosed crest angle of the limiting profile of standing waves, *Wave Motion* 28 (1998) 79–87.
- [17] J. Wilkening, Breakdown of self-similarity at the crests of large amplitude standing water waves, *Phys. Rev. Lett* 107 (2011) 184501.
- [18] P. Concus, Standing capillary–gravity waves of finite amplitude: Corrigendum, *J. Fluid Mech.* 19 (1964) 264–266.
- [19] J.-M. Vanden-Broeck, *Gravity–Capillary Free–Surface Flows*, Cambridge University Press, Cambridge, 2010.
- [20] G. Iooss, P. I. Plotnikov, J. F. Toland, Standing waves on an infinitely deep perfect fluid under gravity, *Arch. Rat. Mech. Anal.* 177 (2005) 367–478.
- [21] B. Rayleigh, On waves, *Philos. Mag.* 1 (1876) 257–279.
- [22] I. Tadjbakhsh, J. B. Keller, Standing surface waves of finite amplitude, *J. Fluid Mech.* 8 (1960) 442–451.
- [23] P. Concus, Standing capillary–gravity waves of finite amplitude, *J. Fluid Mech.* 14 (1962) 568–576.
- [24] P. Plotnikov, J. Toland, Nash-moser theory for standing water waves, *Arch. Rat. Mech. Anal.* 159 (2001) 1–83.
- [25] W. Craig, C. E. Wayne, Newton’s method and periodic solutions of nonlinear wave equations, *Comm. Pure Appl. Math* 46 (1993) 1409–1498.
- [26] J. Bourgain, Nonlinear Schrodinger equations. In *Hyperbolic equations and frequency interactions*, American Mathematical Society, Providence, 1999.
- [27] J.-M. Vanden-Broeck, L. W. Schwartz, Numerical calculation of standing waves in water of arbitrary uniform depth, *Phys. Fluids* 24 (5) (1981) 812–815.
- [28] M. Okamura, M. Ioualalen, C. Kharif, Standing waves on water of uniform depth: on their resonances and matching with short-crested waves, *J. Fluid Mech.* 495 (2003) 145–156.
- [29] M. Okamura, Almost limiting short-crested gravity waves in deep water, *J. Fluid Mech.* 646 (2010) 481–503.
- [30] C. J. Amick, J. F. Toland, The semi-analytic theory of standing waves, *Proc. Roy. Soc. Lond. A* 411 (1987) 123–138.
- [31] E. J. Doedel, H. B. Keller, J. P. Kernévez, Numerical analysis and control of bifurcation problems: (II) Bifurcation in infinite dimensions, *Int. J. Bifurcation and Chaos* 1 (1991) 745–772.
- [32] H. B. Keller, *Numerical Methods for Two-Point Boundary-Value Problems*, Blaisdell, New York, 1968.
- [33] J. Stoer, R. Bulirsch, *Introduction to Numerical Analysis*, 3rd Edition, Springer, New York, 2002.

- [34] J. Guckenheimer, B. Meloon, Computing periodic orbits and their bifurcations with automatic differentiation, *SIAM J. Sci. Comput.* 22 (3) (2000) 951–985.
- [35] D. M. Ambrose, J. Wilkening, Computation of time-periodic solutions of the Benjamin–Ono equation, *J. Nonlinear Sci.* 20 (3) (2010) 277–308.
- [36] D. M. Ambrose, J. Wilkening, Global paths of time-periodic solutions of the Benjamin–Ono equation connecting pairs of traveling waves, *Comm. App. Math. and Comp. Sci.* 4 (1) (2009) 177–215.
- [37] D. M. Ambrose, J. Wilkening, Computation of symmetric, time-periodic solutions of the vortex sheet with surface tension, *Proc. Nat. Acad. Sci.* 107 (8) (2010) 3361–3366.
- [38] M. O. Williams, J. Wilkening, E. Shlizerman, J. N. Kutz, Continuation of periodic solutions in the waveguide array mode-locked laser, *Physica D* 240 (22) (2011) 1791–1804.
- [39] C. G. Broyden, The convergence of a class of double-rank minimization algorithms, Parts I and II, *J. Inst Maths Applics* 6 (1970) 76–90, 222–231.
- [40] J. Nocedal, S. J. Wright, *Numerical Optimization*, Springer, New York, 1999.
- [41] J. Yu, A local construction of the Smith normal form of a matrix polynomial, and time-periodic gravity-driven water waves, Ph.D. thesis, University of California, Berkeley (May 2010).
- [42] J. Wilkening, Stability of solitary water wave collisions and standing waves, (in preparation).
- [43] M. S. Longuet-Higgins, E. D. Cokelet, The deformation of steep surface waves on water. I. a numerical method of computation, *Proc. Royal Soc. A* 350 (1976) 1–26.
- [44] G. R. Baker, D. I. Meiron, S. A. Orszag, Generalized vortex methods for free-surface flow problems, *J. Fluid Mech.* 123 (1982) 477–501.
- [45] R. Krasny, Desingularization of periodic vortex sheet roll-up, *J. Comput. Phys.* 65 (1986) 292–313.
- [46] G. R. Baker, C. Xie, Singularities in the complex physical plane for deep water waves, *J. Fluid Mech.* 685 (2011) 83–116.
- [47] T. Y. Hou, J. S. Lowengrub, M. J. Shelley, Removing the stiffness from interfacial flows with surface tension, *J. Comput. Phys.* 114 (1994) 312–338.
- [48] H. D. Ceniceros, T. Y. Hou, Dynamic generation of capillary waves, *Phys. Fluids* 11 (5) (1999) 1042–1050.
- [49] T. Y. Hou, J. S. Lowengrub, M. J. Shelley, Boundary integral methods for multicomponent fluids and multiphase materials, *J. Comput. Phys.* 169 (2001) 302–362.
- [50] G. Baker, A. Nachbin, Stable methods for vortex sheet motion in the presence of surface tension, *SIAM J. Sci. Comput.* 19 (5) (1998) 1737–1766.
- [51] A. L. Dyachenko, V. E. Zakharov, E. A. Kuznetsov, Nonlinear dynamics on the free surface of an ideal fluid, *Plasma Phys. Rep.* 22 (1996) 916–928.
- [52] W. Artiles, A. Nachbin, Nonlinear evolution of surface gravity waves over highly variable depth, *Phys. Rev. Lett.* 93 (2004) 234501.
- [53] P. A. Milewski, J.-M. Vanden-Broeck, Z. Wang, Dynamics of steep two-dimensional gravity–capillary solitary waves, *J. Fluid Mech.* 664 (2010) 466–477.
- [54] G. B. Whitham, *Linear and Nonlinear Waves*, Wiley, New York, 1974.
- [55] R. S. Johnson, *A modern introduction to the mathematical theory of water waves*, Cambridge University Press, Cambridge, UK, 1997.
- [56] A. D. D. Craik, The origins of water wave theory, *Ann. Rev. Fluid Mech.* 36 (2004) 1–28.

- [57] A. D. D. Craik, George Gabriel Stokes on water wave theory, *Ann. Rev. Fluid Mech.* 37 (2005) 23–42.
- [58] W. Craig, C. Sulem, Numerical simulation of gravity waves, *J. Comput. Phys.* 108 (1993) 73–83.
- [59] Y. W. Lim, P. B. Bhat, V. K. Prasanna, Efficient algorithms for block-cyclic redistribution of arrays, in: *IEEE Symposium on Parallel and Distributed Processing*, 1996, pp. 74–83.
- [60] E. Hairer, S. P. Norsett, G. Wanner, *Solving Ordinary Differential Equations I: Nonstiff Problems*, 2nd Edition, Springer, Berlin, 2000.
- [61] T. Y. Hou, R. Li, Computing nearly singular solutions using pseudo-spectral methods, *J. Comput. Phys.* 226 (2007) 379–397.
- [62] A. Dutt, L. Greengard, V. Rokhlin, Spectral deferred correction methods for ordinary differential equations, *BIT* 40 (2) (2000) 241–266.
- [63] J. Huang, J. Jia, M. Minion, Accelerating the convergence of spectral deferred correction methods, *J. Comput. Phys.* 214 (2006) 633–656.
- [64] A. T. Layton, M. L. Minion, Implications of the choice of quadrature nodes for Picard integral deferred corrections methods for ordinary differential equations, *BIT Numerical Mathematics* 45 (2005) 341–373.
- [65] J. Wilkening, Hybrid spectral deferred correction methods that crossover to pure Picard iteration, Tech. rep., Lawrence Berkeley National Laboratory, (in preparation) (2012).
- [66] M. O. Williams, E. Shlizerman, J. Wilkening, J. N. Kutz, The low dimensionality of time-periodic standing waves in water of finite and infinite depth, *SIAM J. Appl. Dyn. Syst.*(accepted).
- [67] L. F. Shampine, Some practical Runge–Kutta formulas, *Mathematics of Computation* 46 (1986) 135–150.
- [68] M. Lu, B. He, Q. Luo, Supporting extended precision on graphics processors, *Proceedings of the Sixth International Workshop on Data Management on New Hardware* (2010) 19–26.
- [69] Y. Hida, X. S. Li, D. H. Bailey, The qd package for double-double and quad-double arithmetic, <http://crd-legacy.lbl.gov/~dhbailey/mpdist/> (2003–2012).
- [70] J.-M. Vanden-Broeck, Nonlinear gravity-capillary standing waves in water of arbitrary uniform depth, *J. Fluid Mech.* 139 (1984) 97–104.
- [71] B. Chen, P. G. Saffman, Steady gravity-capillary waves on deep water–I. weakly nonlinear waves, *Studies in Appl. Math.* 60 (1979) 183–210.
- [72] T. J. Bridges, Secondary bifurcation and change of type for three-dimensional standing waves in finite depth, *J. Fluid Mech.* 179 (1987) 137–153.
- [73] B. F. Akers, W. Gao, Wilton ripples in weakly nonlinear model equations, *Comm. Math. Sci.* 10 (3) (2012) 1015–1024.
- [74] L. Bauer, H. B. Keller, E. L. Raiss, Multiple eigenvalues lead to secondary bifurcation, *SIAM Review* 17 (1) (1975) 101–122.
- [75] M. Ioualalen, C. Kharif, Stability of three-dimensional progressive gravity waves on deep water to superharmonic disturbances, *Eur. J. Mech. B* 12 (1993) 401–414.
- [76] M. Ioualalen, A. J. Roberts, C. Kharif, On the observability of finite-depth short-crested water waves, *J. Fluid Mech.* 322 (1996) 1–19.
- [77] P. Deuffhard, A. Hohmann, *Numerical Analysis in Modern Scientific Computing, An Introduction*, 2nd Edition, Springer, New York, 2003.
- [78] J. Wilkening, An infinite branching hierarchy of time-periodic solutions of the Benjamin–Ono equation–[ArXiv:0811.4209](https://arxiv.org/abs/0811.4209).

- [79] G. G. Stokes, Considerations relative to the greatest height of oscillatory irrotational waves which can be propagated without change of form, in: *Mathematical and physical papers*, Vol. 1, Cambridge University Press, 1880, pp. 225–228.
- [80] A. D. D. Craik, George Gabriel Stokes on water wave theory, *Annual Rev. Fluid Mech.* 37 (2005) 23–42.
- [81] M. S. Longuet-Higgins, M. J. H. Fox, Theory of the almost-highest wave: the inner solution, *J. Fluid Mech.* 80 (4) (1977) 721–741.
- [82] M. S. Longuet-Higgins, M. J. H. Fox, Theory of the almost-highest wave. part 2. matching and analytic extension, *J. Fluid Mech.* 85 (4) (1978) 769–786.
- [83] C. J. Amick, L. E. Fraenkel, J. F. Toland, On the Stokes conjecture for the wave of extreme form, *Acta Math.* 148 (1) (1982) 193–214.
- [84] D. V. Maklakov, Almost-highest gravity waves on water of finite depth, *Euro. J. Appl. Math.* 13 (2002) 67–93.
- [85] I. S. Gandzha, V. P. Lukomsky, On water waves with a corner at the crest, *Proc. R. Soc. A* 463 (2007) 1597–1614.
- [86] D. G. Crapper, An exact solution for progressive capillary waves of arbitrary amplitude, *J. Fluid Mech.* 2 (1957) 532–540.
- [87] J.-M. Vanden-Broeck, A new family of capillary waves, *J. Fluid Mech.* 98 (1) (1980) 161–169.
- [88] F. Dias, T. J. Bridges, The numerical computation of freely propagating time-dependent irrotational water waves, *Fluid Dynamics Research* 38 (2006) 803–830.
- [89] N. I. Muskhelishvili, *Singular Integral Equations*, 2nd Edition, Dover, New York, 1992.
- [90] A. I. Van de Vooren, A numerical investigation of the rolling up of vortex sheets, *Proc. Royal Soc. London Ser. A* 373 (1980) 67–91.
- [91] D. I. Pullin, Numerical studies of surface-tension effects in nonlinear Kelvin–Helmholtz and Rayleigh–Taylor instabilities, *J. Fluid Mech.* 119 (1982) 507–532.
- [92] M. O. Williams, E. Shlizerman, J. Wilkening, J. N. Kutz, The low dimensionality of time-periodic standing waves in water of finite and infinite depth, *SIAM J. Appl. Dyn. Syst.*(accepted).